



#### Available online at www.sciencedirect.com

### **ScienceDirect**

Geochimica et Cosmochimica Acta

Geochimica et Cosmochimica Acta 308 (2021) 237-255

www.elsevier.com/locate/gca

# The structure of natural biogenic iron (oxyhydr)oxides formed in circumneutral pH environments

Andrew H. Whitaker <sup>a,1</sup>, Robert E. Austin <sup>a</sup>, Kathryn L. Holden <sup>a</sup>, Jacob L. Jones <sup>b</sup>, F. Marc Michel <sup>c</sup>, Derek Peak <sup>d</sup>, Aaron Thompson <sup>e</sup>, Owen W. Duckworth <sup>a,\*</sup>

a Department of Crop and Soil Sciences, North Carolina State University, Raleigh, NC 27695, USA
 b Department of Materials Science and Engineering, North Carolina State University, Raleigh, NC 27695, USA
 c Department of Geosciences, Virginia Tech, Blacksburg, VA 24060, USA
 d Department of Soil Science, University of Saskatchewan, Saskatoon, Saskatchewan S7N 5A8, Canada
 c Department of Crop and Soil Sciences, University of Georgia, Athens, GA 30602, USA

Received 3 December 2020; accepted in revised form 31 May 2021; Available online 8 June 2021

#### Abstract

Biogenic iron (Fe) (oxyhydr)oxides (BIOS) partially control the cycling of organic matter, nutrients, and pollutants in soils and water via sorption and redox reactions. Although recent studies have shown that the structure of BIOS resembles that of two-line ferrihydrite (2LFh), we lack detailed knowledge of the BIOS local coordination environment and structure required to understand the drivers of BIOS reactivity in redox active environments. Therefore, we used a combination of microscopy, scattering, and spectroscopic methods to elucidate the structure of BIOS sampled from a groundwater seep in North Carolina and compare them to 2LFh. We also simulated the effects of wet-dry cycles by varying sample preparation (e.g., freezing, flash freezing with freeze drying, freezing with freeze drying and oven drying). In general, the results show that both the long- and short-range ordering in BIOS are structurally distinct and notably more disordered than 2LFh. Our structure analysis, which utilized Fe K-edge X-ray absorption spectroscopy, Mössbauer spectroscopy, X-ray diffraction, and pair distribution function analyses, showed that the BIOS samples were more poorly ordered than 2LFh and intimately mixed with organic matter. Furthermore, pair distribution function analyses resulted in coherent scattering domains for the BIOS samples ranging from 12-18 Å, smaller than those of 2LFh (21-27 Å), consistent with reduced ordering. Additionally, Fe L-edge XAS indicated that the local coordination environment of 2LFh samples consisted of minor amounts of tetrahedral Fe(III), whereas BIOS were dominated by octahedral Fe(III), consistent with depletion of the sites due to small domain size and incorporation of impurities (e.g., organic C, Al, Si, P). Within sample sets, the frozen freeze dried and oven dried sample preparation increased the crystallinity of the 2LFh samples when compared to the frozen treatment, whereas the BIOS samples remained more poorly crystalline under all sample preparations. This research shows that BIOS formed in circumneutral pH waters are poorly ordered and more environmentally stable than 2LFh.

© 2021 Elsevier Ltd. All rights reserved.

Keywords: Ferrihydrite; Structure; X-ray spectroscopy; X-ray Scattering; Mössbauer spectroscopy; Iron oxidizing bacteria; Environmental minerology

<sup>\*</sup> Corresponding author.

E-mail address: owen duckworth@ncsu.edu (O.W. Duckworth).

<sup>&</sup>lt;sup>1</sup> Current address: Department of Plant and Soil Sciences, Oklahoma State University, 371 Agricultural Hall, Stillwater, OK 74078, USA.

#### 1. INTRODUCTION

The sorption and redox reactivity of iron (Fe) oxides, hydroxides, and oxyhydroxides (referred to in the paper as "(oxyhydr)oxides") partially controls the mobility of nutrients, and contaminants (e.g., Pb, Cr, As) in engineered and natural systems (Benjamin and Leckie, 1981; Cornell and Schwertmann, 2003; Jambor and Dutrizac, 1998; Waychunas et al., 2005; Xu et al., 2012), and the storage of carbon in soils (Kahle et al., 2002; Kiem and Kögel-Knabner, 2002; Rasmussen et al., 2018; Torn et al., 1997; Wagai and Mayer, 2007). Recent documentation of the widespread formation of biogenic iron (oxyhydr)oxides (BIOS) under suboxic conditions and at redox gradients (Druschel et al., 2008; Roden et al., 2012; Roden, 2012) in diverse terrestrial and aquatic environments, including surface water (Jones, 1975; Lünsdorf et al., 1997; Sheldon and Skelly, 1990), drains (Emerson and Moyer, 2002; Houot and Berthelin, 1992), wetlands (Emerson and Weiss, 2004; Neubauer et al., 2002; Weiss et al., 2005), groundwater (Emerson and Moyer, 1997; Tuhela et al., 1997), springs (Emerson and Revsbech, 1994a,b), and mines (Chan et al., 2004; Swanner et al., 2011), has led to a growing recognition of their importance in regulating key biogeochemical processes.

Many studies (Ferris, 2005; Ferris et al., 2000; Kennedy et al., 2003; Sowers et al., 2017; Whitaker and Duckworth, 2018; Whitaker et al., 2018) have shown that BIOS mineralogy resembles two-line ferrihydrite (2LFh), a commonly utilized and extensively studied Fe (oxyhydr)oxide that is an effective sorbent of DOM, nutrients, and metals (Jambor and Dutrizac, 1998); however, the differences in composition and formation mechanisms alter BIOS mineral structure and reactivity relative to pure synthetic analogues, such as 2LFh. Recent studies have determined BIOS sorption capacities for solutes (Field et al., 2019; Kennedy et al., 2011; Kikuchi et al., 2019; Langley et al., 2009a; Rentz et al., 2009; Sowers et al., 2017; Sowers et al., 2019; Whitaker and Duckworth, 2018; Whitaker et al., 2018) can vary dramatically from those of synthetic 2LFh. These differences in reactivity have been attributed to the presence of organic moieties (e.g., phosphoryl, carboxylic acid, phenolic, and amines) in biomolecules (Kennedy et al., 2011; Langley et al., 2009b; Sowers et al., 2019; Suga et al., 2017) within the BIOS, as well as structural properties (specific surface area (SSA), coherent scattering domain size (CSDs) and structural ordering) (Cismasu et al., 2011; Field et al., 2019; Michel, 2014; Sowers et al., 2017; Whitaker et al., 2018).

Over the past 25 years, the structure of synthetic 2LFh has been a topic of intense debate (Combes et al., 1990; Combes et al., 1989; Drits et al., 1993; Manceau, 2009; Manceau, 2010; Manceau and Drits, 1993; Manceau and Gates, 1997; Michel et al., 2010a; Michel et al., 2007a; Michel et al., 2007b; Michel et al., 2010b; Rancourt and Meunier, 2008), leading to two distinct structural models. The first ("Dritz model") (Drits et al., 1993) is composed of three phases, a defective ferrihydrite phase, a defect free ferrihydrite phase, and small portions of ultra-dispersed hematite with coherent scattering domains (CSDs) in the

10–20 Å range with all phases composed of 100% octahedral Fe(III). The second ("Michel model") (Michel et al., 2010a, 2007a) is composed of a 13 unit Fe(III) structure that has a central tetrahedral Fe(III) unit and the remainder octahedral (Michel et al., 2010a, 2007b). Recent X-ray absorption spectroscopy (Maillot et al., 2011; Mikutta, 2011; Peak and Regier, 2012) and scattering (Harrington et al., 2011) studies have confirmed the presence of tetrahedral Fe(III) in synthetic 2LFh. Despite the intense interest in the structure of 2LFh, only five studies (Cismasu et al., 2011; Michel, 2014; ThomasArrigo et al., 2014; Toner et al., 2012; Toner et al., 2009) have provided detailed structural characterization of BIOS and or natural ferrihydrite, of which two of the studies used samples collected from hydrothermal vents at Juan de Fuca Ridge.

Motivated by the broad occurrence and distinct reactivity of BIOS, the goal of this study was to elucidate the structure, degree of structural order, and morphology of BIOS by utilizing a suite of spectroscopic and scattering techniques (Fe L-edge and K-edge X-ray absorption spectroscopy (XAS), high energy X-ray total scattering and pair distribution functions (PDF), and Mössbauer spectroscopy (MBS)) and compare the results to synthetic 2LFh, which has been extensively studied (Chadwick et al., 1986; Cismasu et al., 2012; Cismasu et al., 2014; Drits et al., 1993; Hiemstra, 2013; Maillot et al., 2011; Manceau and Gates, 1997; Michel et al., 2010a, 2007b; Mikutta, 2011; Peak and Regier, 2012; Wang et al., 2016; Zhao et al., 1994). Furthermore, structural differences in BIOS as a result of aging and wet-dry cycles were simulated by varying sample preparation (e.g. freezing, oven drying, and lyophilization), which provides insights on the structural stability, and possible persistence, of BIOS in aquatic environments.

#### 2. METHODS

### 2.1. BIOS Collection and Preparation, and Stream Water Sampling

Biogenic iron (oxyhydr)oxides (Supplementary Fig. S1) were sampled in March of 2016 from a small tributary off of Walnut Creek (35°45'47"N 78°41'51"W; Raleigh, North Carolina) where fluffy, orange mats of BIOS have been observed throughout the year on the water surface to a depth of 5 cm (creek depth = 5-10 cm) when water flow is slow (Almaraz et al., 2017; Field et al., 2019). These BIOS are composed of biogenic and abiogenic iron (oxyhydr)oxides that have been sorbed to or precipitated with bacterial cells, cellular derived organic matter, allochthonous dissolved organic matter, and other impurities (e.g., Al, Si, P) (Chan et al., 2004; Chan et al., 2009; Druschel et al., 2008; Sowers et al., 2019). Previous research conducted in similar areas (ground water seeps in the North Carolina Piedmont) have shown the presence of filamentous and tube-like structures within the BIOS morphology (Almaraz et al., 2017; Sowers et al., 2017; Sowers et al., 2019; Whitaker and Duckworth, 2018), indicative of iron (oxyhydr)oxides produced by iron oxidizing bacteria (Chan et al., 2004; Chan et al., 2009; Druschel et al.,

2008; Emerson and Revsbech, 1994a). Dissolved oxygen concentrations taken from the previously sampled BIOS mats ranged from 34-134 μM O<sub>2</sub> (Whitaker et al., 2018; Field et al., 2019), similar to other field sites where BIOS formations have been observed (Druschel et al., 2008; Emerson and Weiss, 2004; Mitsunobu et al., 2012). Disposable polypropylene (PP) syringes were used to collect and place the BIOS into multiple 500 mL PP storage bottles. The BIOS were allowed to settle, and the water was decanted. This collection-decanting process occurred 5 more times until ample BIOS were collected. A small portion of the BIOS were put into a 15 mL PP conical centrifuge tube and flash frozen at -70 °C in a homebuilt portable dry-ice bath (Jensen and Lee, 2000). Stream water was sampled with 60 mL PP syringes and placed into 125 mL PP storage bottles after using a disposable 0.22 µm nylon filter (VWR International). Measurements for stream water pH (pH = 6.23) and temperature (20.0 °C) were taken at a depth of 2.5 cm below the water surface, directly within the BIOS mats. All PP syringes and storage bottles were acid washed with 1 M HCl and triple-rinsed with DI H<sub>2</sub>O. All water samples were analyzed within 24 hours according to the methods stated in Section 2.3 (See below).

All samples were then taken to the laboratory. The flash frozen BIOS sample was immediately freeze-dried and stored in the freezer at -20 °C until further analyses, whereas the rest of the BIOS samples were centrifuged for 10 min at 10,000g. The supernatant was decanted and the BIOS were pooled into one 50 mL PP centrifuge tube and suspended in DI, which was then vortexed (Vortex Genie 2, Scientific Industries) to ensure adequate homogenization. The BIOS were centrifuged one last time at 10,000g for 10 min. The supernatant was disposed of, and the resulting composite sample was subdivided into three equal parts. Four different BIOS preparation techniques were employed to look at their effects on the BIOS structure. Sample (Fr) was stored as a frozen paste in the freezer at -20 °C. Sample (FrFD) was frozen as a wet paste at -20 °C and then freeze-dried. The FrFD sample treatment is a common preparation technique for synthetic two-line ferrihydrite as well as other iron oxyhydr(oxides) (Schwertmann and Cornell, 2008) and was therefore included as a BIOS treatment. Sample (OD) was oven-dried at 55 °C and serves as an upper limit for BIOS mineralogy transformations in the environment via drying. Sample (FFFD) refers to the flash frozen freeze-dried sample. Prior to sample preparation, a 250 mg subsample of the BIOS paste was oven-dried for 24 hours at 100 °C to be used to determine the elemental composition. All samples were homogenized via vigorous vortexing (BIOS Fr) or finely ground with an agate mortar and pestle (BIOS FrFD, FFFD, and OD) then stored in the freezer at -20 °C in the dark until further analyses.

#### 2.2. Two-line Ferrihydrite (2LFh) Synthesis.

Two-line ferrihydrite was synthesized in the laboratory with procedures established by Schwertmann and Cornell (Schwertmann and Cornell, 2008). Briefly, a 0.331 M solution of Fe(NO)<sub>3</sub>·9H<sub>2</sub>O in DI was neutralized with 1 M

KOH addition while under vigorous mixing on a stir plate. The pH of the suspension was held constant at  $7.5 \pm 0.5$  for 30 minutes before transferring into multiple 50 mL PP centrifuge tubes. The ferrihydrite suspensions were then centrifuged at 10,000g for 10 min, the supernatant was discarded and the resulting 2LFh was rinsed with DI. This centrifuge-rinse cycle was repeated four more times. The 2LFh suspensions were combined into one 50 mL PP centrifuge tube, raised to volume with DI, and centrifuged a final time at 10,000g for 10 min. The supernatant was discarded and the 2LFh paste was divided into three equal proportions. For synthetic 2LFh, three different sample preparation techniques were utilized in order to look at their impact on the structure of synthetic 2LFh relative to the BIOS. Sample (Fr) was stored as a frozen paste in the freezer at -20 °C. Sample (FrFD) was frozen as a wet paste at -20 °C proceeded by freeze-drying. Sample (OD) was oven-dried at 55 °C. A 250 mg wet 2LFh paste was ovendried for 24 h at 100 °C in order to determine the percent of iron in the solid. All samples were homogenized via vigorous vortexing (2LFh Fr) or finely ground with an agate mortar and pestle (2LFh FrFD and OD) then stored in the freezer at -20 °C in the dark until further analyses.

#### 2.3. Mineral and stream water characterization

Both BIOS and synthetic 2LFh were analyzed for elemental composition. Ten milligrams of dry BIOS were used for the determination of the C and N content via total combustion using a Perkin Elmer Series II-2400 CHNS/O analyzer. Metals, P, and S concentrations in the BIOS were determined by dissolving 50 mg of dry solids with 10 mL each of concentrated trace metal HCl and HNO3 acid, and then diluting to 40 mL with DI. The digestions were hand shaken and incubated at room temperature for one hour before filtration through 0.22 um nylon filters (VWR International). The BIOS filtrates were then analyzed for Fe, Mn, Al, Ca, Si, K, Mg, Na, Cu, Pb, Zn, S, and P by using a Perkin Elmer Optima 8000 Inductively Coupled Plasma-Optical Emission Spectrometer (ICP-OES), whereas the synthetic two-line ferrihydrite filtrate was analyzed for iron. Ferrous iron stabilized within the BIOS was extracted with 4 M HCl acid. The digestate was filtered with a 0.22 μm nylon filter (VWR International) and analyzed for Fe(II) using a VWR V-1200 series UV-visible spectrophotometer according to the Stookey method (Stookey, 1970).

The stream water sample was divided into three equal aliquots before analyses. The first was acidified to a pH < 2 using trace metal grade nitric acid and analyzed for Fe, Mn, Al, Ca, Si, K, Mg, Na, Cu, Pb, Zn, S, and P byICP-OES. The second was acidified to a pH < 2 with trace metal grade hydrochloric acid and analyzed for dissolved organic carbon (DOC) via a Shimadzu total organic carbon analyzer. The final aliquot was analyzed for NH<sub>4</sub><sup>+</sup>, NO<sub>3</sub><sup>-</sup>, PO<sub>4</sub><sup>3</sup>-, SO<sub>4</sub><sup>2</sup>-, and Cl<sup>-</sup> using a Lachat Quick Chem 8000 series flow injection analyses system (FIAS). The water samples were acidified within 1 hour of field sampling, stored at 4 °C, and analyzed within 24 hours of stream water collection to limit changes in elemental concentrations, especially DOC (Norrman, 1993).

#### 2.4. Scanning electron microscopy

Samples of freeze dried (FrFD) and oven dried (OD) BIOS and 2LFh were imaged by using FEI Verios 460L Field Emission Scanning Electron Microscope at 50–20,000× magnification. Samples were mounted on carbon tape and imaged at a pressure of  $9.63 \times 10^{-5}$  Pa and a transmission level of 3 kV.

#### 2.5. K-edge X-ray absorption spectroscopy

Iron K-edge spectra were collected at beamline 11-2 at the Stanford Synchrotron Radiation Lightsource (SSRL). All BIOS and synthetic 2LFh samples were loaded onto aluminum sample holders as wet pastes or dry solids and sealed with kapton tape. All Fe K-edge spectra were collected at room temperature in fluorescence mode with a passivated implanted planar silicon (PIPS) detector, respectively. Monochromator energy was calibrated by adjusting the first derivative maximum of the Fe foil to the element binding energy of 7112 eV. The incident beam was energy selected using a Si (2 2 0) double-crystal monochromator, and higher-order harmonics were rejected with a rhodium coated mirror. Fluorescence spectra were collected using Soller slits and a Mn filter. Three spectra were collected for each sample, with no evidence of beam damage in successive scans, and averaged to improve the signal-to-noise ratio.

Spectra were energy calibrated, averaged, backgroundsubtracted, and splined as described by Kelly et al. (2008) using the SIXPACK interface (Webb, 2005), which makes use of the IFEFFIT code (Newville, 2001). To determine the oxidation state of the 2LFh and BIOS samples, linear combination fits (LCFs) of the Fe K-edge X-ray absorption near edge structure (XANES) spectra were performed from 7100 to 7200 eV using vivianite and ferrihydrite, which serve as ferrous and ferric iron mineral standards, respectively. Extended X-ray absorption fine structure (EXAFS) fluorescence spectra were fit by linear combination fitting using iron mineral standards to investigate the BIOS and synthetic 2LFh mineral phase and structure. Based off of previous XAS LCFs of 2LFh and BIOS (Field et al., 2019; Sowers et al., 2017; Whitaker and Duckworth, 2018; Whitaker et al., 2018) initial linear combination fits started with the two-line ferrihydrite and HFO mineral standard for the 2LFh and BIOS samples, respectively, with additional mineral standards added one-by-one and retained if its contribution was greater than 10% of the LCF. The iron mineral standards that made up less than 10% of the linear combination fit were removed, and fits were recalculated using the remaining standards. All iron mineral standards (Harrington et al., 2012a; Harrington et al., 2012b; Morris and Hesterberg, 2012; O'Day et al., 2004) used in the linear combination fits are listed in Supplementary Table S1, with the bolded standards being the ones used for the final fits. Further details on iron mineral standard preparation can be found in the Supplementary Information. All LCF fits are normalized to 100%, with the raw summation ranging from 99 to 100  $\pm$  1% for XANES and  $100 \pm 15\%$  for EXAFS.

Shell-by-shell structural fits for the synthetic 2LFh and BIOS samples were performed on the K-edge EXAFS spectra using SIXPACK (Webb, 2005). All spectra were modeled with parameters from the EXAFS equation. First shell (Fe-O) and second shell (Fe-Fe edge- and cornersharing) single scattering paths were generated from hematite (CrystalMaker<sup>®</sup> 9.2.7 Software) using Feff9 (Rehr et al., 2010). The amplitude reduction factor  $(S_0^2)$  was set to 0.83 (Liu and Hesterberg, 2011; Wang et al., 2016) for all shells. The threshold energy correction factor ( $\Delta E_0$ ) was allowed to float during optimization but was linked to a common value for every path considered for each sample. The Debye-Waller parameters ( $\sigma^2$ ) of the Fe-O (0.011 Å<sup>2</sup>) and Fe-Fe paths (0.013 Å<sup>2</sup>) were obtained from initial fits of the samples and fixed for the final fits to facilitate comparison of the first and second shell coordination numbers (CN) and interatomic distances (R) of the synthetic 2LFh and BIOS samples. Due to the presence of Fe(III) bound to organic matter in the BIOS samples, an additional path (Fe-C), generated from Fe(III)-protochelin (a catecholate complex) (Harrington et al., 2012b), was incorporated into the model to test for improvement. The  $\sigma^2$  value for the Fe-C path  $(0.01 \text{ Å}^2)$  was determined from initial fits, and fixed for the final structural fits. All  $\sigma^2$  values were within the ranges of reported literature values (Harrington et al., 2012b; Liu and Hesterberg, 2011; Wang et al., 2016). Significance of structural model improvement was tested for both Fe—Fe paths and the Fe—C path. Only paths that were significant at the 95% confidence interval (Downward et al., 2007; Hamilton, 1965) were reported.

#### 2.6. L-edge X-ray absorption spectroscopy

Iron L-edge XANES analyses were performed at the Spherical Grating Monochromator (SGM) beamline of the Canadian Light Source in Saskatoon, SK according to a previously established protocol (Peak and Regier, 2012). Briefly, all Fe L<sub>2,3</sub>-edge spectra were obtained using inverse partial fluorescence yield (IPFY), which is a bulk sensitive analysis that is free of self-absorption effects (Achkar et al., 2011) by scanning from 700 to 735 eV in 0.1 eV steps . All BIOS and synthetic 2LFh samples were homogenized with an agate mortar and pestle, then placed onto graphite tape. To investigate the bulk structure, IPFY measurements were taken using an energy resolving silicon drift yield detector that monitored the partial fluorescent yield (PFY) of the O Kα emission as the incident photon energy was scanned through the Fe L<sub>II</sub> and L<sub>III</sub> absorption threshold. The calculated IPFY was obtained by taking the inverse of the O PFY after normalization to the incident photon flux as recorded by a gold mesh. Further details on the quantitation of IPFY can be found in reference (Peak and Regier, 2012).

#### 2.7. X-ray total scattering

X-ray total scattering experiments were conducted at the Advanced Photon Source, Argonne National Laboratory on beam line 11-ID-B. For these analyses, all BIOS and synthetic 2LFh samples were packed and sealed as wet

pastes (Fr samples) or powders (FrFD, OD, FFFD samples) into ~1 mm Kapton capillaries. All data were collected at ambient temperature using a Perkin Elmer amorphous silicon detector and with an X-ray energy of ~59 keV  $(\lambda = 0.2113 \text{ Å})$ . Total scattering data for PDF analysis were collected with a sample-to-detector distance of ~16 cm. Synchrotron X-ray diffraction measurements were collected at a longer distance of ~60 cm. A CeO<sub>2</sub> standard was used to calibrate the experimental geometry. The raw 2-D scattering data were integrated and converted to 1-D intensity vs wave vector (O) spectra using Fit2D software (Hammersley, 1997). A polarization correction factor (0.95) was applied during the integration process. Single crystal diffraction spots from the samples and detector artifacts were masked prior to integrating the raw data. This masking procedure has been used in other total scattering experiments (Cismasu et al., 2011) and did not significantly affect the data. The total scattering structure function S(O), reduced structure function F(Q), and the pair distribution function PDF were obtained using the program PDFgetX3 (Juhás et al., 2013). The total scattering structure function S (Q) was obtained by normalizing the BIOS and synthetic 2LFh to their elemental compositions (Supplementary Table S2). The PDF or G(r) was obtained by Fourier transforming the S(Q), with a  $Q_{max} = 26 \text{ Å}^{-1}$ . Details about the minerals short-, medium-, and long-range structural order can be determined from the PDF. The average coherent scattering domain sizes (CSD) can also be estimated based off of the distance r(A) at which the PDF signal-to-noise ratio attenuates to one (Gilbert et al., 2004; Michel et al., 2007b). Errors for CSDs are estimated at  $\pm 3$  Å (Hall et al., 2000).

#### 2.8. <sup>57</sup>Fe Mössbauer spectroscopy

All cryogenic temperatures (140, 77, 35, 5 K) of <sup>57</sup>Fe Mössbauer spectra for the BIOS and synthetic 2LFh where collected in transmission mode using a variable temperature He-cooled system with a 1024 channel detector. A <sup>57</sup>Co source (~50 mCi or less) embedded in a Rh matrix was used at room temperature. Samples were mounted between two pieces of 0.127 mm thickness Kapton tape and transferred to the spectrometer cryostat immediately at 140 K or less. The velocity (i.e., gamma-ray energy) range for all experiments was  $\pm$  11 mm s<sup>-1</sup> and provided a detection limit of 0.1-1% Fe. Velocity was calibrated with a <sup>57</sup>Fe foil at RT and all center shifts (CSs) and peak positions are stated with respect to this standard. The transducer ran in constant accelerating mode and all data were folded to achieve a flat background. The fitting of all Mössbauer spectra was performed using the Voigt-based fitting (VBF) method of Rancourt and Ping (Rancourt and Ping, 1991) for quadrupole splitting distributions (QSDs) and combined hyperfine field distributions (HFDs), as implemented in the Recoil TM software, ISA Inc. All VBF Mössbauer parameter definitions and a description of the relevant notation are given by Rancourt and Ping (Rancourt and Ping, 1991). Further details regarding the Mössbauer spectral analysis and fitting approach can be found in the Supplementary Information.

#### 3. RESULTS

The elemental concentrations within the BIOS, synthetic 2LFh, and the stream water are presented in Supplementary Tables S2 and S3. The C (9.5%) and Fe (27.3%) contents of BIOS, which have been correlated with sorption reactivity, are near the average composition (8.5% and 22.1%, respectively) of 14 samples collected from the North Carolina Piedmont region (Field et al., 2019). Trace metal concentrations are also similar to those reported previously for field collected natural Fe (oxyhydr)oxides (Cismasu et al., 2011; Whitaker and Duckworth, 2018).

Scanning Electron Microscope (SEM) images of two dried samples (frozen and freeze dried, FrFD; and oven dried, OD) 2LFh and BIOS samples are shown in Fig. 1. Both 2LFh FrFD (Fig. 1A) and OD (Fig. 1B) samples consist of irregularly shaped aggregates, in good agreement with other studies (Cismasu et al., 2013; Sowers et al., 2017; Whitaker et al., 2018), suggesting only minor morphological change occurred between FrFD and OD drying techniques for 2LFh. In contrast, the BIOS FrFD sample (Fig. 1C and D) is composed of poorly-defined aggregates with numerous sheaths, indicative of BIOS produced by Leptothrix sp. (Duckworth et al., 2009; Fleming et al., 2011; Jones, 1975; Prigsheim, 1949). Interestingly, the BIOS OD sample morphology (Fig. 1E) appear to be similar in morphology to 2LFh samples (Fig. 1A and B). However, higher magnification images of the BIOS OD sample (Fig. 1F) reveal microbial sheaths that appear to be fused into larger aggregates, suggesting morphological changes stemming from the drying method in the BIOS OD.

Synchrotron X-ray diffractograms (S-XRD) of the 2LFh and BIOS samples are shown in Fig. 2. For the synthetic 2LFh samples, two main maxima occur at d-spacings of ~2.55 and ~1.50 Å, characteristic of ferrihydrite (Cornell and Schwertmann, 2003). A visual comparison between synthetic 2LFh sample preparations shows broadened maxima that are shifted towards higher d-spacings for the 2LFh frozen (Fr) sample consistent with higher structural disorder and/or smaller crystallite size (Michel et al., 2007b) when compared to the dried samples FrFD and OD. Minimal variation occurs between FrFD and OD samples of 2LFh, suggesting no significant structural differences are induced by the two drying methods. Within the BIOS samples, we see changes with sample treatment. For Fr, FrFD, and the FFFD samples, a broad peak appears at ~4.70 Å that is not present in the BIOS OD pattern. Additionally, a broad peak centered at ~3.3 Å is dominant for the BIOS Fr sample but is reduced in amplitude or absent in the samples that were dried. In the BIOS samples, a number of sharp peaks consistently appear in the pattern that indicate crystalline impurities that can be attributed predominantly to quartz (qz) and kaolinite (k). The differences in relative intensity of these mineral peaks may be to either sample heterogeneity, and/or drying and preparation effects.

Pair distribution functions derived from X-ray total scattering are displayed in Fig. 3. The coherent scattering domain (CSD) sizes can be estimated by using the attenuation in peak amplitudes with increasing distance (*r*) (Fig. 3a). Estimated CSDs for 2LFh Fr, FrFD, and OD

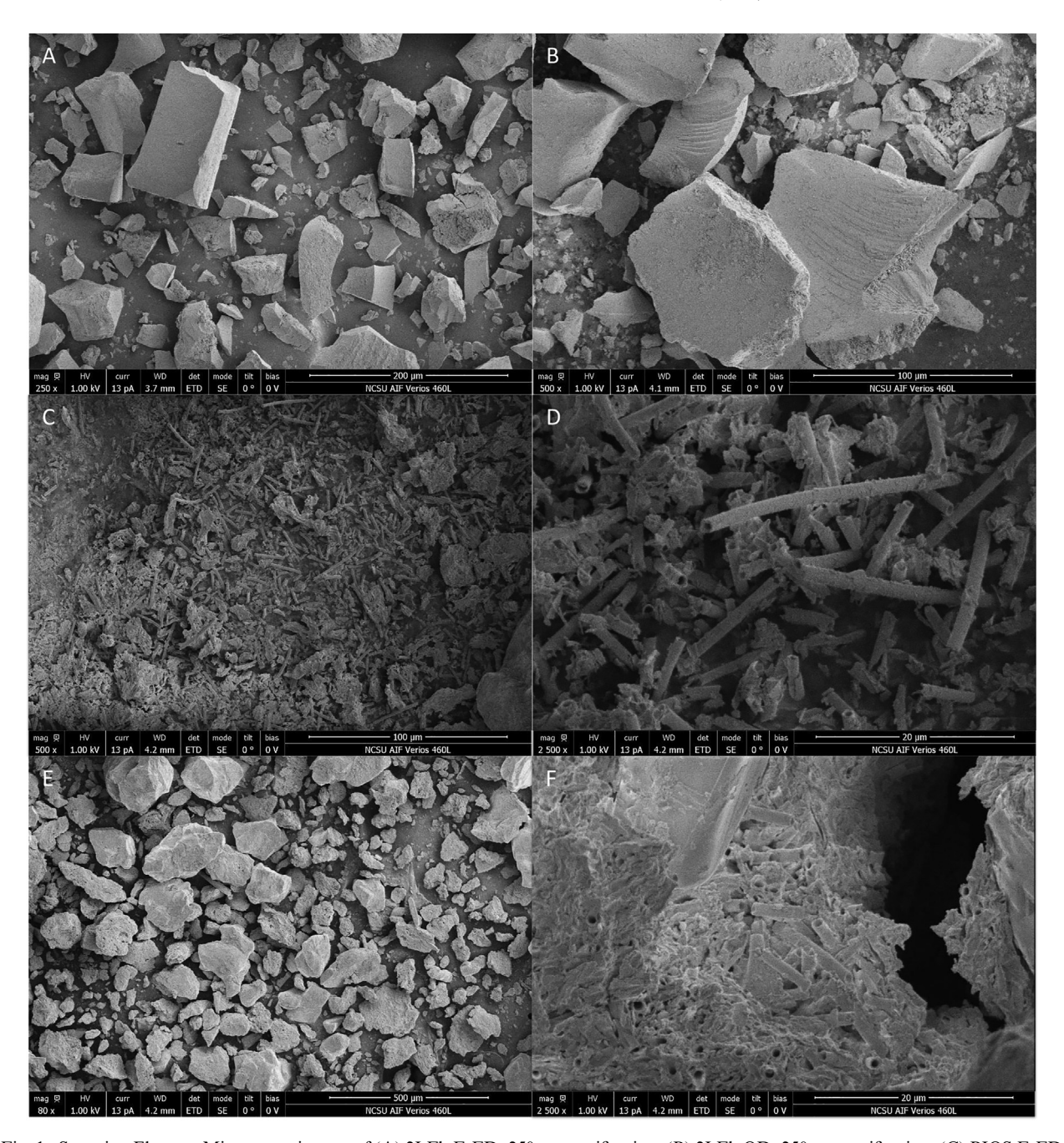


Fig. 1. Scanning Electron Microscopy images of (A) 2LFh FrFD; 250× magnification, (B) 2LFh OD; 250× magnification, (C) BIOS FrFD; 250× magnification, (E) 250× magnification, (E) BIOS OD; 250× magnification.

samples were 21, 27, and 27 Å, respectively, which are consistent with CSDs obtained for synthetic ferrihydrite (Michel et al., 2007b; Toner et al., 2012; Wang et al., 2016; Whitaker et al., 2018). All BIOS PDFs attenuate at shorter radial distances r(Å) (18 Å for BIOS Fr, FrFD, and OD, and 12 Å for FFFD). Comparison of the shortrange order (0–5 Å) of the 2LFh and BIOS PDF samples are shown in Fig. 3B, with prominent peaks identified via vertical black dashed lines. For all samples, similar peak positions occur at ~2.0, 3.05, and 3.45 Å, which correspond

to atomic pair distances of Fe—O, edge sharing Fe—Fe, and corner-sharing Fe—Fe, respectively. Little if any variation is seen between 2LFh samples. However, many differences are seen between BIOS and 2LFh samples, and amongst BIOS samples. In all BIOS samples, substantial dampening in the Fe—Fe corner-sharing peak occurs when compared to all 2LFh samples. Within the BIOS samples, peaks at ~1.5 Å and ~1.60 Å have been interpreted as average distances between bonded (e.g., C—C/N/O) and un-bonded atoms within the organic matter (Poulain et al., 2019) and

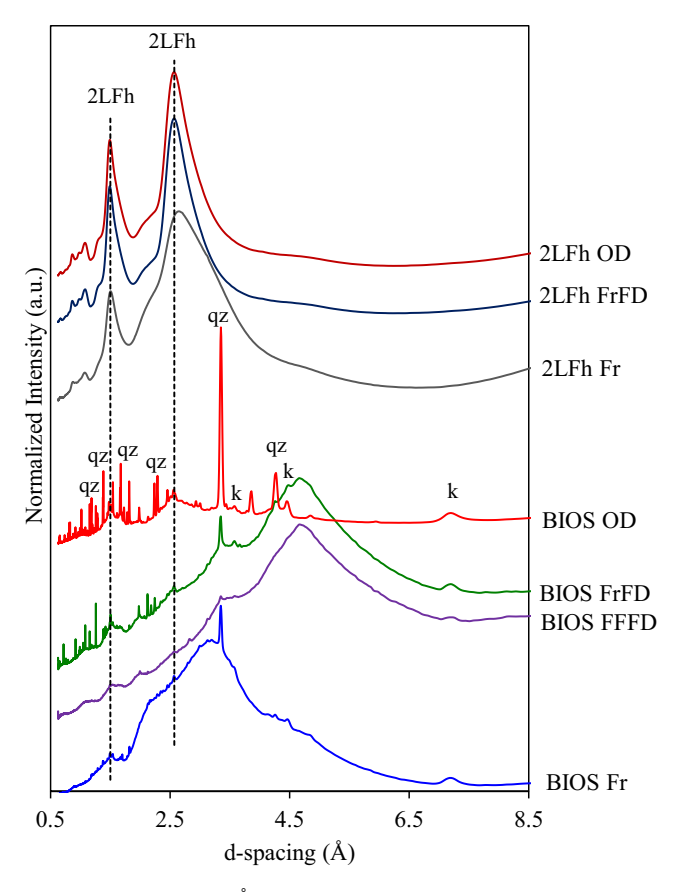


Fig. 2. Synchrotron X-ray diffraction (S-XRD;  $\lambda = 0.2113~\text{Å}$ ) patterns of synthetic 2LFh and BIOS sample preparations. Vertical dashed lines represent the two main 2LFh diffraction peaks. The main diffraction peaks arising due to crystalline impurities in the BIOS diffraction patterns are denoted by "qz" and "k" for quarts and kaolinite, respectively.

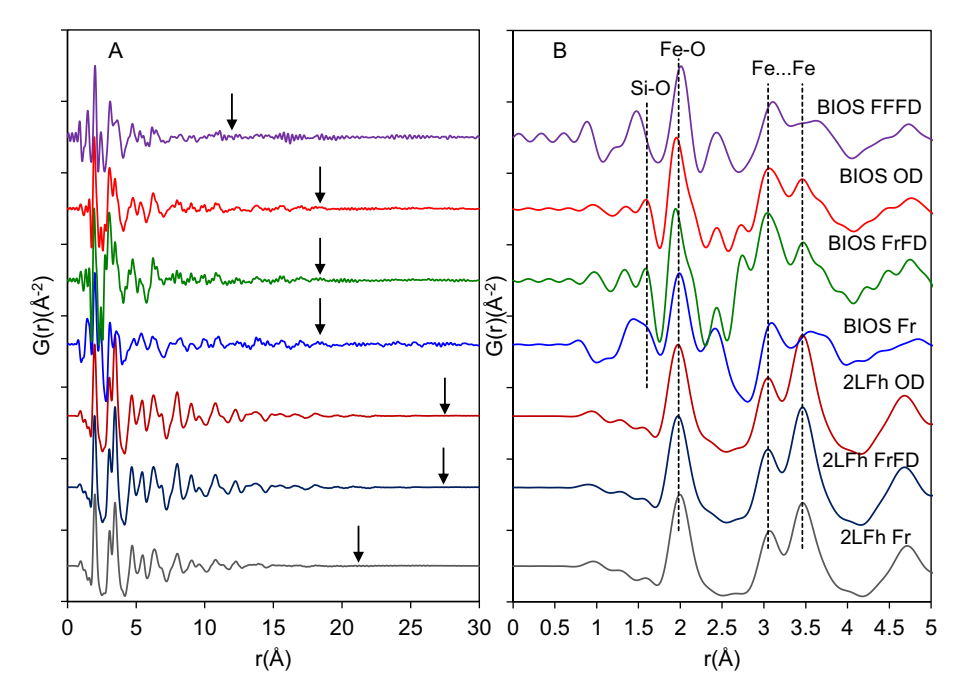


Fig. 3. Pair distribution functions (PDF) (A) and comparison of the short-range order (B) obtained for the synthetic 2LFh and BIOS sample preparations. Coherent scattering domain (CSD) sizes (Å) are denoted by the solid black arrows.

mineral surface associated and/or precipitates of tetrahedral silica (Cismasu et al., 2011; Toner et al., 2012), respectively.

Mössbauer spectra (Supplementary Figs. S2-S4) for 2LFh may be fit with a single population of Fe(III)-(oxyhydr)oxides with spectral parameters (CS ~ 0.47 mm s  $^{-1}$ , QS ~  $\pm 0.01$  mm s<sup>-1</sup>, and peak Bhf ~ 50 T at 5 K; Supplementary Tables S4-S7) that are consistent with ferrihydrite standards(Cornell and Schwertmann, Eusterhues et al., 2008). All 2LFh samples are very shortrange-ordered (SRO) and do not start to magnetically order until the temperature is at or below 77 K, but are all fully ordered at 5 K (Supplementary Table S7). Sample preparation has a significant influence on the 2LFh ordering, which is especially evident in the 35 K spectra (Fig. 4). At 35 K, the Fe population in the 2LFh OD samples is nearly all magnetically ordered, while the preparation technique best preserving the initial state, 2LFh Fr has 66% of its Fe population in the vicinity of their blocking temperature (T<sub>N</sub>) as evidenced by a collapsed sextet [(b)OxHy)], whereas the 2LFh FrFD sample is intermediate of those two and displays distinct sextet lines for ~1/3 of the Fe population, whereas the remainder is above the blocking temperature and displays a doublet (dblt) feature. This gradient in ordering between the samples is also evident in the average hyperfine field strength (Bhf) at 5 K, which varies from 47.6 to 48.1 to 48.9 for the 2LFh Fr, 2LFh FrFD, and 2LFh OD samples, respectively. Note that the peak saturation hyperfine field strength — essentially the field strength at full magnetic ordering — is similar for all samples, ranging from 49.4(8) to 49.7(1) to 50.7(5) in the 2LFh Fr, 2LFh FrFD, and 2LFh OD samples, respectively, which indicates the fundamental mineral structure is similar for all samples, but that the 2LFh Fr sample, for instance, has a distribution of magnetic ordering that is skewed toward more disorder than the 2LFh OD samples. This observation is consistent with Wang et al. (2016) who have shown that 2LFh samples exhibit similar ranges in magnetic ordering

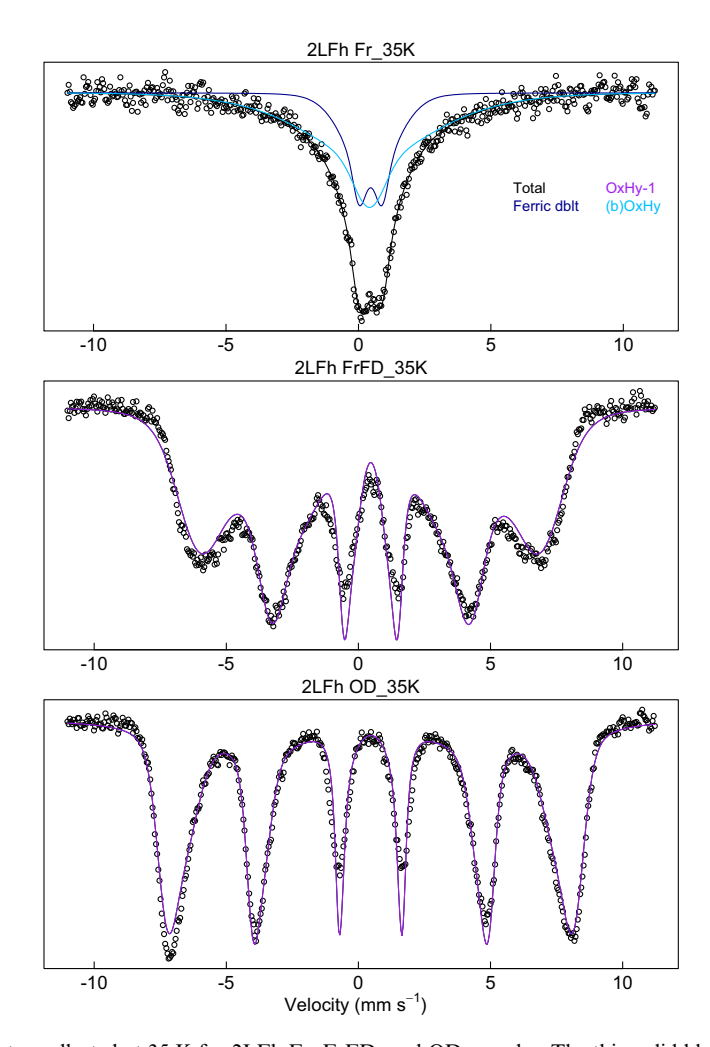


Fig. 4. Mössbauer (MBS) spectra collected at 35 K for 2LFh Fr, FrFD, and OD samples. The thin solid black line is the total calculated fit, through the discrete data points (black open face circles) and the solid colored lines represent the MBS model fits (see legend). Detailed fitting parameters are listed in Supplementary Information Tables S4–S6. The y-axes are count intensities (arbitrary units), and the x-axes are source velocities (mm s<sup>-1</sup>). Doublets (dblt) are indicated as either ferric or ferrous; Oxyhydroxide sextets (OxHy-1 and OxHy-2) are numbered when they have sufficiently distinct parameter values; Collapsed sextets that are near their blocking temperature are given as (b)OxHy.

temperature and the degree of transition from a doublet to a collapsed sextet to a full sextet (in their case at 20 K) is a function of particle size.

Mössbauer spectra for BIOS are shown in Supplementary Figs. S5–S8, with spectral parameters listed in Supplementary Tables S7–S11. The bulk of the Fe(III)-(oxyhydr) oxide population in the BIOS samples is best approximated by a very disordered ferrihydrite-like phase, such that the hyperfine field strength is depressed to ~45 T even at 5 K (Supplementary Table S7) and, in the most disordered sample prep (BIOS Fr), ~18% of the Fe population remains blocked, exhibiting a collapsed sextet [(b)OxHy].

As with the 2LFh, sample preparation affected the ordering of the BIOS samples, although here our selection of the collection temperature is less ideal to illustrate this effect. All samples magnetically order between 35 K and 5 K (Fig. 5), and likely exhibit some range of ordering temperature. This is somewhat evident even at 35 K where the amount of blocked Fe [i.e., Fe in a collapsed sextet, (b) OxHy component] varies from 13(1)% in the BIOS OD sample to 8.1(5) in the BIOS FrFD sample to none in the BIOS Fr and BIOS FFFD samples (Fig. 5; Supplementary Tables S8–S11). However, we can also examine the average and peak Bhf at 5 K (Supplementary Table S7), where Fe populations of lower crystallinity would exhibit lower peak Bhf values. We find the average Bhf to be 44.8, 44.3, 43.2, and 43.1 and the peak Bhf to be 46.5(6), 45.8(2), 45.2(6), and 44.7(9), for the BIOS OD, BIOS FrFD, BIOS FFFD, and BIOS Fr, respectively, results similar to Bhf values obtained for highly disordered BIOS that formed in marine environments (e.g., ~44-47 T) (Toner et al., 2012). In all cases, the order of crystallinity is the same with the BIOS OD exhibiting the highest crystallinity and the BIOS Fr exhibiting the lowest.

In the BIOS samples, we observe one paramagnetic ferrous Fe contribution (Q-Fe<sup>II</sup>-1) that is consistent with Fe (II) sorbed to clays, Fe(III) (oxyhydr)oxides or in organic complexes based on MB spectral parameters (CS ~ 1 mm/ s; QS  $\sim$  3 mm/s) comprising between 1 and 2% of the spectral area (Thompson et al., 2011). Interestingly, these BIOS QS values are larger than ones seen for Fe(II) bound to Al/ Fe oxyhydr(oxides) and clays (QS  $\sim 2.8 \text{ mm s}^{-1}$ ) (Larese-Casanova et al., 2010; Schaefer et al., 2011; Williams and Scherer, 2004), and approach values seen for Fe(II) bound to fulvic acid (QS  $\sim$ 3.1 mm s<sup>-1</sup>) and bacterial cells (QS  $\sim$  3. 2-3.3 mm s<sup>-1</sup>) (Chen and Thompson, 2018; Rancourt et al., 2005). This phase was resolved in all preparations of the BIOS samples at 35 K and above, except the BIOS FFFD (which had a higher signal to noise due to lower sample loading into the cryostat) where it was only detected at 35 K. The spectral fraction of Fe(II) detected by Mössbauer spectroscopy agrees well with the 1.1% Fe(II) determined by HCl acid digestion followed by the ferrozine assay listed in Supplementary Table S2. Interestingly, we also detected a small population (~3%) of Fe(III)-(oxyhydr)oxides that order near 77 K and/or 35 K with MB spectral parameters (CS  $\sim 0.47$  mm s<sup>-1</sup>, QS  $\sim -0.12$  mm s<sup>-1</sup>, and Bhf  $\sim 48$  T at 35 K) that are most similar to nanogoethite standards (Supplementary Tables S8-S11). Similar MB spectral phases have been determined to occur along a Fe redox gradient

in highly weathered basaltic soils with substantial amounts of organic matter (Thompson et al., 2011). This minor phase (OxyHy-2) is detected in all BIOS samples, except the BIOS FFFD sample that had low signal-to-noise. The absence of nanogoethite in S-XRD data and EXAFS LCFs (vida infra) likely arises due to the lower sensitivity (~5%) of these techniques.

X-ray absorption near edge structure (XANES) spectra, and EXAFS k-space spectra and their Fourier Transforms (FTs) of the 2LFh and BIOS samples are shown in Supplementary Fig. S9, with LCFs shown as overlain black dashed lines. XANES LCFs (Supplementary Fig. S9A) for all 2LFh and the BIOS samples were best fit with 100% two-line ferrihydrite, indicating all samples lack Fe (II) (<10%) as a fit component, consistent with the low Fe(II) concentrations seen in chemical digestions (Supplementary Table S2) and Mössbauer spectra (Supplementary Tables S8-S11) of the BIOS, as well as other studies (Whitaker and Duckworth, 2018; Whitaker et al., 2018). EXAFS LCFs (Supplementary Fig. S9B and Table 1) revealed all 2LFh samples were composed of 100  $\pm$  1% two-line ferrihydrite with no change in mineralogy between sample treatments (Table 1). In contrast, BIOS samples were best fit with differing combinations of 2LFh, hydrous ferric oxide (HFO; a freshly precipitated and highly disordered phase), and Fe(III)-peat (predominantly mononuclear, organic-bound Fe(III) (Morris and Hesterberg, 2012))

Shell-by-shell structural model fits of the EXAFS and FT Magnitude plots are shown as overlain black dashed lines in Fig. 6A and B, respectively, with fit parameters shown in Table 2. In general, 2LFh are fit with a Fe—O shell at 1.96-1.98 Å, and two Fe-Fe shells at  $\sim 3.03-3.05$ and 3.46 Å, corresponding to Fe(III)-O, Fe-Fe edgesharing, and Fe-Fe corner-sharing distances, respectively (Michel et al., 2007b; Toner et al., 2012). These bond distances are consistent with peak positions seen in PDFs (Fig. 3B). Similar main features are observed in the BIOS samples, which are best fit with Fe-O shell at 1.98-2.00 Å and a Fe-Fe shells at ~3.05-3.07 Å. An additional Fe-C shell at ~2.83 Å provides statistical improvement of the fits for the Fr and FFFD samples, consistent with the representation of a Fe(III)-peat standard in LCF fits and of MBS parameters suggesting the presence of an Fe mineral-organic matter phases in the BIOS samples. The Fe—C shell did not provide a statistical improvement of the fits for BIOS FrFD or OD samples (Downward et al., 2007; Hamilton, 1965).

All 2LFh and BIOS samples Fe L-edge XANES spectra are plotted in Fig. 7. Consistent with Peak and Regier (2012), all spectra have well resolved L<sub>-III</sub> and L<sub>-II</sub> edges located between 706–713 eV and 718–725 eV, respectively (Fig. 7A), with additional splitting of the main L-edge peaks due to Fe 3d and O 2p orbitals that are sensitive to the coordination environment. For comparison, stacked L<sub>-III</sub> edge spectra for 2LFh (Fr, FrFD, and OD) and BIOS (Fr, FrFD, OD, and FFFD) are plotted with hematite (black dotted line) and maghemite (black dashed line) in Fig. 7B. For hematite, substantial splitting of the L<sub>-III</sub> edge into two well resolved peaks occur at ~708 and 709.5 eV

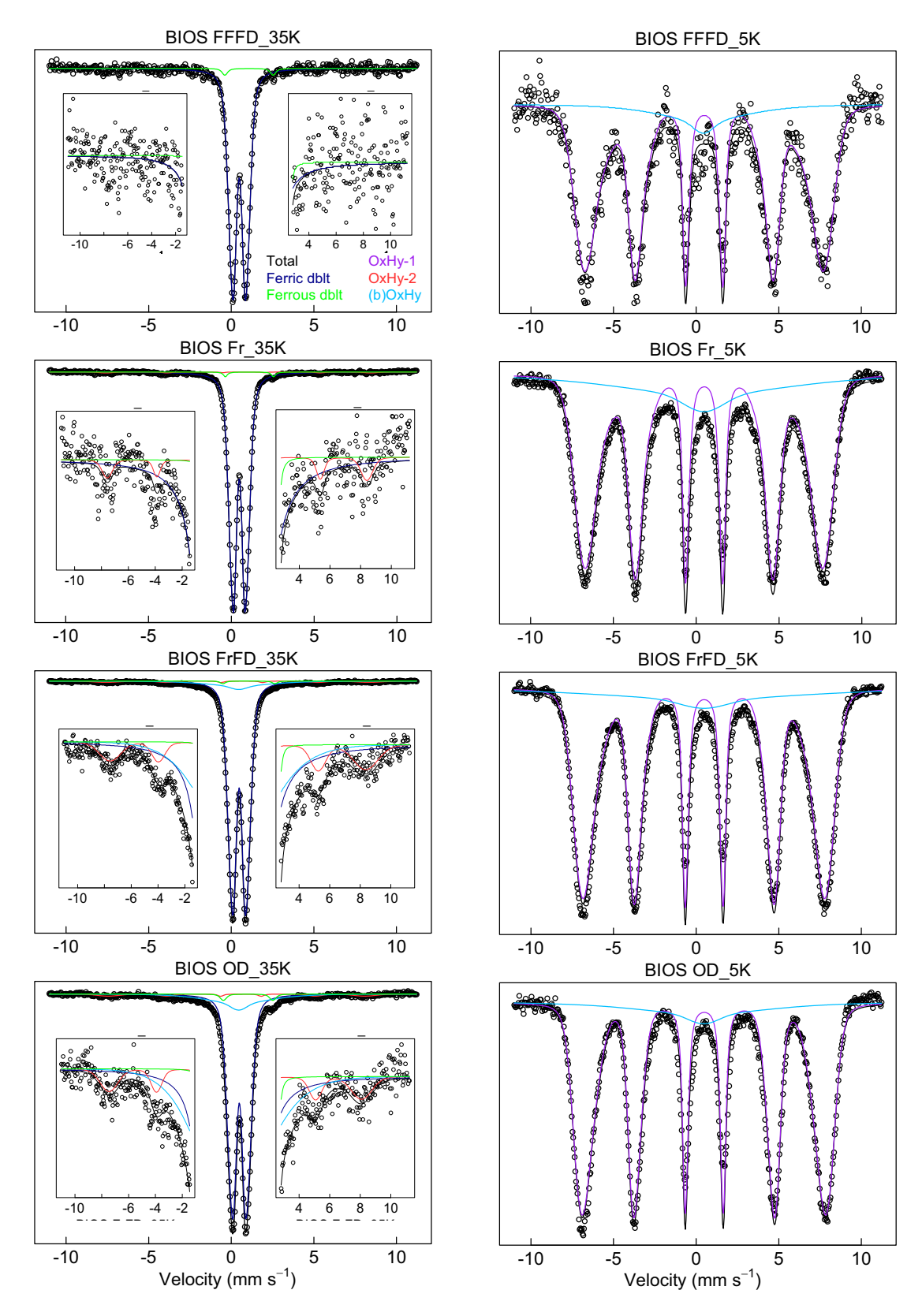


Fig. 5. Mössbauer (MBS) spectra collected at 35 K for BIOS FFFD, Fr, FrFD, and OD samples. The thin solid black line is the total calculated fit, through the discrete data points (black open face circles) and the solid colored lines represent the MBS model fits (see legend). Detailed fitting parameters are listed in Supplementary Information Tables S8–S11. The y-axes are count intensities (arbitrary units), and the x-axes are source velocities (mm s<sup>-1</sup>). Doublets (dblt) are indicated as either ferric or ferrous; Oxyhydroxide sextets (OxHy-1 and OxHy-2) are numbered when they have sufficiently distinct parameter values; Collapsed sextets that are near their blocking temperature are given as (b) OxHy.

Table 1 Fe K-edge EXAFS linear combination fits (LCFs) for 2LFh and BIOS sample preparations. LCFs were normalized to 100%, with raw fits summing to  $100\pm15\%$ .

Sample ID	Component	% Contribution	R-value
Fh Fr Fh FrFD Fh OD	2-Line Ferrihydrite 2-Line Ferrihydrite 2-Line Ferrihydrite	$100 \pm 1$ $100 \pm 1$ $100 \pm 1$	0.0236 0.0056 0.0165
BIOS Fr	HFO Fe(III)-peat	$79 \pm 3$ $21 \pm 3$	0.0393
BIOS FrFD	2-Line Ferrihydrite HFO Fe(III)-peat	$55 \pm 7$ $29 \pm 6$ $16 \pm 2$	0.0215
BIOS OD	2-Line Ferrihydrite HFO Fe(III)-peat	$53 \pm 6$ $31 \pm 5$ $16 \pm 2$	0.0194
BIOS FFFD	2-Line Ferrihydrite HFO Fe(III)-peat	$39 \pm 7$ $34 \pm 6$ $27 \pm 2$	0.0244

and is typical for minerals having 100% octahedral Fe(III) as their only coordination environment. However, maghemite has a substantial decrease in L<sub>-III</sub> edge splitting as well as minor broadening in the main L<sub>-III</sub> peak, which has been attributed to the presence of tetrahedral Fe(III) (Crocombette et al., 1995). Therefore, a visual comparison of the splitting of the L<sub>-III</sub> peaks along with their respective peak intensity ratios can be used as a qualitative analysis of the minerals coordination environment (Peak and Regier, 2012). For all 2LFh samples, substantial decreases in the splitting of the L<sub>-III</sub> edge peaks occur with changes in the relative intensities between the two L<sub>-III</sub> peaks, as well as

broadening of the main L<sub>-III</sub> edge peak, consistent with Fe(III) in tetrahedral and octahedral coordination (Peak and Regier, 2012). Interestingly, all BIOS sample spectra look nearly identical to the hematite standard, with only slight decreases in L<sub>-III</sub> peak splitting compared to the hematite standard, which suggests BIOS are primarily composed of Fe(III) in octahedral coordination with only minor amounts of Fe(III) in tetrahedral coordination (i.e., less tetrahedral Fe(III) than 2LFh). It is important to note that sample disorder and variations in the ligands involved may also affect the Fe L<sub>-III</sub> edge spectra (Peak and Regier, 2012). Similar results were obtained by Mikutta (Mikutta, 2011) who showed that Fe(III)-organic matter coprecipitates were nearly 100% octahedral Fe(III) using Fe K-edge XANES spectroscopy.

#### 4. DISCUSSION

## 4.1. Long range ordering and domain size — S-XRD, PDF, and MBS approaches

Several of the approaches used, including S-XRD, PDF analysis, and MBS, can be used to determine structural information, a length scale >5 nm (e.g., long range ordering). The S-XRD data reveals differences between the BIOS and 2LFh samples. In diffractograms for all BIOS samples, dampening in maxima intensities at d-spacings of ~2.55 and ~1.50 Å are consistent with enhanced structural strain and/or smaller coherent domain sizes (CSD) (Michel et al., 2007b). Similar results have been obtained via extended X-ray absorption fine-structure spectroscopy (EXAFS) and X-ray total scattering studies for synthetic 2LFh synthesized in the presence of Si and Al, and for other BIOS and natural iron (oxyhydr)oxides when compared to pure

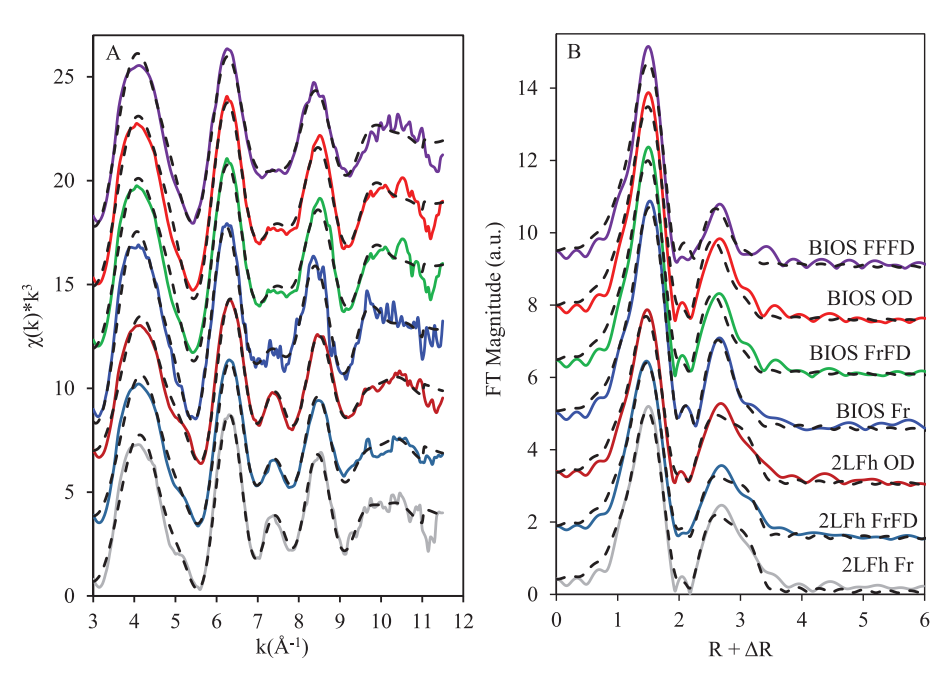


Fig. 6. Fe K-edge (a) extended X-ray absorption fine structure (EXAFS) spectra, and (b) FT magnitude plots of the 2LFh and BIOS sample preparations. Shell-by-shell structural fits are represented by overlain dashed lines.

Table 2 Structural fit parameters for the synthetic 2LFh and BIOS samples.

Sample	Path	N	R (Å)	$\sigma^2 (\mathring{A}^2)$	$\Delta E_0 (eV)$	R-factor
Fh Fr	Fe—O	5.47 (0.39)	1.98 (0.01)	0.011	2.16 (2.06)	0.0198
	Fe—Fe	2.60 (0.60)	3.05 (0.02)	0.013		
	Fe—Fe	2.40 (0.87)	3.46 (0.03)	0.013		
Fh FrFD	Fe—O	5.26 (0.37)	1.97 (0.01)	0.011	1.80 (2.15)	0.0214
	Fe—Fe	2.03 (0.56)	3.05 (0.02)	0.013		
	Fe—Fe	2.19 (0.81)	3.46 (0.03)	0.013		
Fh OD	Fe—O	5.03 (0.36)	1.96 (0.01)	0.011	1.19 (2.23)	0.0199
	Fe—Fe	2.21 (0.54)	3.03 (0.02)	0.013		
	Fe—Fe	2.33 (0.79)	3.46 (0.03)	0.013		
BIOS Fr	Fe—O	6.54 (0.28)	2.00 (0.01)	0.011	4.44 (1.01)	0.0092
	Fe—Fe	3.49 (0.34)	3.08 (0.01)	0.013	, ,	
	Fe—C	1.93 (0.47)	2.82 (0.04)	0.01		
BIOS FrFD	Fe—O	6.51 (0.44)	1.98 (0.01)	0.011	2.45 (1.82)	0.0296
	Fe—Fe	3.03 (0.56)	3.05 (0.02)	0.013		
	Fe—C	Not Sig.				
BIOS OD	Fe-O	6.50 (0.44)	1.98 (0.01)	0.011	2.59 (1.83)	0.0302
	Fe—Fe	3.03 (0.57)	3.05 (0.02)	0.013	` ,	
	Fe—C	Not Sig.				
BIOS FFFD	Fe—O	6.08 (0.42)	1.99 (0.01)	0.011	2.98 (1.62)	0.0255
	Fe—Fe	2.31 (0.50)	3.07 (0.03)	0.013	` ,	
	Fe—C	1.85 (0.96)	2.83 (0.08)	0.01		

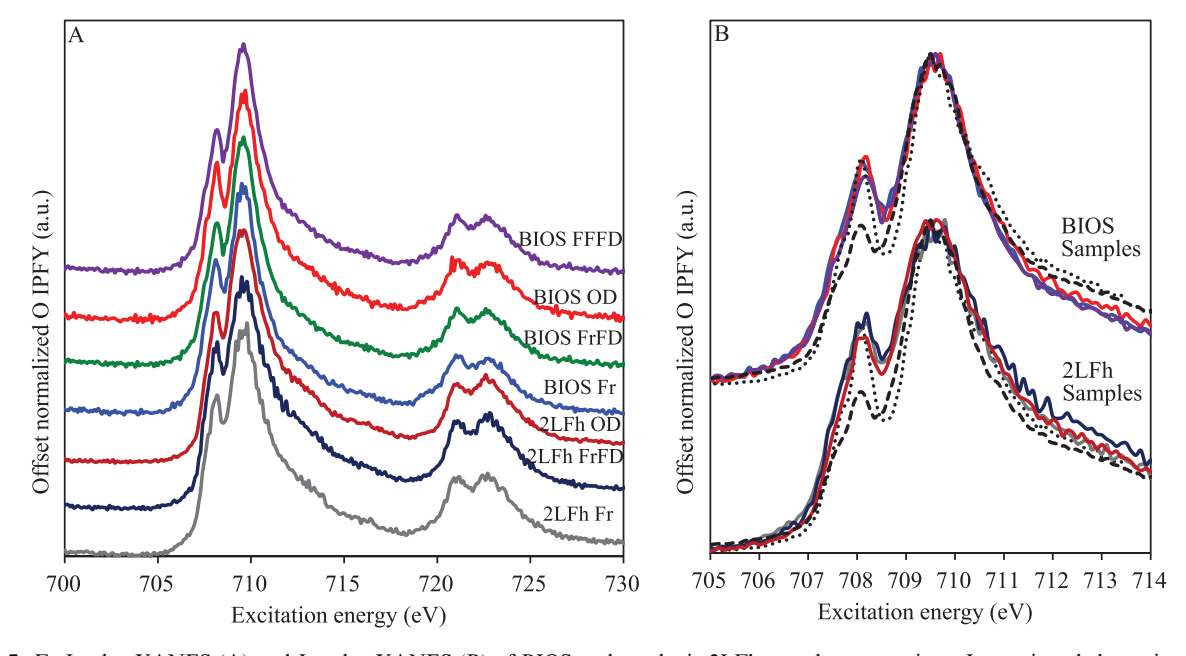


Fig. 7. Fe L-edge XANES (A) and  $L_3$ -edge XANES (B) of BIOS and synthetic 2LFh sample preparations. Iron minerals hematite (black dotted line) and maghemite (black dashed line) were used as references for 100% octahedral Fe(III) and mixed octahedral/tetrahedral Fe(III), respectively. The spectral color notation used to label the samples is the same for both (A) and (B).

synthetic 2LFh (Cismasu et al., 2012; Cismasu et al., 2014; Cismasu et al., 2011; Sowers et al., 2017; Toner et al., 2012; Whitaker and Duckworth, 2018; Whitaker et al., 2018). For the BIOS Fr, FrFD, and FFFD samples, two broad peaks appear at ~3.3 Å and ~4.70 Å that are not present in the BIOS OD pattern. These peaks are likely caused by natural

organic matter (NOM) and are consistent with other XRD studies of high C:Fe ratio and ferrihydrite-OM composites (Chen et al., 2014; Eusterhues et al., 2008; Mikutta et al., 2014; Poggenburg et al., 2016; Rancourt et al., 2005). Variations in peak width at ~3.3 Å for the BIOS Fr sample compared to the BIOS FrFD and FFFD samples occur due to

water in the BIOS Fr sample, which was analyzed as a wet paste. Similar diffraction peaks were seen in a ferritin sample that was suspended in water and analyzed via S-XRD (Michel et al., 2010b).

In MBS, Fe(III)-(oxyhydr)oxides that are blocked or near their blocking temperature (the (b) OxHy component in Supplementary Table S8) at 5 K represent phases so disordered that assigning them to pure mineral phases is perhaps unjustified. The substantial disorder in the BIOS samples is consistent with organic matter-mineral association, foreign ion (Al substitution in the Fe mineral structure, or the presence of adsorbed Si). In a MB spectra, Fe (III) in a discrete, isolated organic matter complex would manifest as a doublet at 5 K; however, if the Fe(III) complexed with the organic matter is structurally part of the mineral then it will manifest as a sextet with the increasing organic matter lowering the ordering temperature and decreasing the hyperfine field strength. We do not observe any doublets at 5 K consistent with discrete Fe-OM complexes and thus the best interpretation MBS data is that nearly all of the Fe atoms in the BIOS samples are involved in the ferrihydrite-like structure to some extent. We have seen similar examples of this when analyzing soil samples by both EXAFS and MBS (Ginn et al., 2017; Herndon et al., 2019) and also have interpreted other MBS spectra of soil samples in this way (Chen et al., 2018; Chen and Thompson, 2018; Coward et al., 2018; Winkler et al., 2018). It is worth noting that we have a relatively high Fe:organic carbon ratio (0.62) as compared to many studies of Fe-organic complexes and synthetic Fe-organic aggregates (Chen et al., 2014; Guénet et al., 2017; Karlsson and Persson, 2012; Mikutta, 2011; ThomasArrigo et al., 2019; Vantelon et al., 2019; Vilgé-Ritter et al., 1999), possibly reducing the occurrence of discrete complexes and oligomers while favoring the formation of a ferrihydrite like phase mixed with organic matter (Chen et al., 2014; Mikutta, 2011; ThomasArrigo et al., 2019).

All BIOS PDFs attenuate at shorter radial distances r (Å) (18 Å for BIOS Fr, FrFD, and OD, and 12 Å for FFFD). The CSD size of BIOS have been linked to the presence of Si, Al, P, and organic matter, which has been shown to decrease ordering and size of natural Fe (oxyhydr)oxides and synthetic 2LFh synthesized with Al, Si, and organic matter (Cismasu et al., 2012; Cismasu et al., 2014; Cismasu et al., 2011; Eusterhues et al., 2008; Mikutta, 2011; Toner et al., 2012; Whitaker et al., 2018). Within the series of BIOS samples, the smaller CSD for the BIOS FFFD sample suggests that flash freezing the BIOS during initial sampling helped preserve its structure as opposed to the three methods of sample preparation that occurred in the lab (Fr, FrFD, and OD). We also note that the larger CSDs for Fr, FrFD, and OD may have also have been influenced by the increased crystalline impurities (qz, k) seen in Fig. 2. Overall, trends from the PDFs, including the CSD size of BIOS compared to 2LFh and the effects of sample treatment on BIOS and 2LFh, are qualitatively consistent with those derived from S-XRD data. Likewise, MBS data indicate that all BIOS samples are considerably less ordered than the 2LFh laboratory sample set based on magnetic ordering temperature and Bhf values (Figs. 4

and 5; Supplementary Figs. S2–S8; Supplementary Tables S4–S11), and consistent with our S-XRD and PDF data, as well as other studies examining the structure of BIOS and ferrihydrite-organic matter co-precipitates when compared to pure synthetic 2LFh (Cismasu et al., 2011; Eusterhues et al., 2008; Mikutta, 2011; Sowers et al., 2017; Toner et al., 2012; Toner et al., 2009; Whitaker and Duckworth, 2018; Whitaker et al., 2018).

#### 4.2. Short-range ordering—XAS and PDF analyses

XAS and PDF data provides specific information about the electron configuration and local coordination environment (e.g., two to three coordination shells for XAS) of atoms in materials. In LCF analyses of EXAFS spectra, all BIOS samples were more poorly ordered than their 2LFh counterparts, as determined by the presence of HFO in fits. In addition, organic complexes are also present in these fits due to the inclusion of Fe(III)-peat standards. Specifically, the LCFs indicate the BIOS Fr as  $79 \pm 3\%$ HFO and 21  $\pm$  3% Fe(III)-peat; the BIOS FrFD and BIOS OD treatments best fit with 2LFh, HFO, and Fe(III)-peat at 55  $\pm$  7%, 29  $\pm$  6%, and 16  $\pm$  2% and 53  $\pm$  6%,  $31 \pm 5\%$ , and  $16 \pm 2\%$ , respectively, suggesting a slight increase in structural ordering compared to the BIOS Fr treatment, as evidenced by an increase in the fraction of ferrihydrite at the expense of HFO. The BIOS FFFD treatment was represented by  $39 \pm 7\%$ ,  $34 \pm 6$ , and  $27 \pm 2\%$ 2LFh, HFO, and Fe(III)-peat, respectively, suggesting perhaps some ordering upon drying as compared to the Fr sample. Interestingly, changes in the % Fe(III)-Peat LCF component may be derived from sample preparation. Desorption studies conducted by Sowers et al. (2019) have shown that up to 20% of the organic C in BIOS can be released using DI water alone. This may account for the decrease from 27% Fe(III)-Peat in BIOS FFFD to 21% Fe(III)-Peat in the BIOS Fr sample. BIOS FrFD and BIOS OD are both 16% Fe(III)-Peat and include higher percentages of ferrihydrite in their LCFs which may be due to the more aggressive drying of the OD sample or longer sample preparation time (i.e., aging) of the FrFD sample compared with the FFFD sample.

When comparing the BIOS EXAFS spectra with the 2LFh spectra (Supplementary Fig. S9), two main differences are noticeable. The absence of a shoulder in the BIOS spectra between  $k = 5-5.5 \text{ Å}^{-1}$  and dampening of the BIOS maximum between  $k = 7-8 \text{ Å}^{-1}$ , which corresponds to a decrease in Fe-O<sub>6</sub> corner-sharing octahedra (Toner et al., 2009), consistent with other EXAFS and total scattering studies of BIOS and natural iron (oxyhydr)oxides (Cismasu et al., 2011; Sowers et al., 2017; Toner et al., 2012; Toner et al., 2009; Whitaker and Duckworth, 2018; Whitaker et al., 2018). The 2LFh and BIOS FT magnitude plots (Supplementary Fig. S9C) show a large first-shell peak at R +  $\Delta$ R = 1.5 Å, consistent with a Fe(III)—O interatomic distance (Shannon, 1976). Second-shell peak positions occur at R +  $\Delta$ R = 2.5 Å and ~3 Å and are characteristic of Fe-Fe distances between edge- and corner-sharing Fe-O<sub>6</sub> octahedra (Michel et al., 2007b; Toner et al., 2009; Wang et al., 2016), respectively. The absence of a Fe-Fe corner-sharing feature in the fits for BIOS spectra is consistent with this diminished amplitude at 3.4 Å in PDFs (Fig. 3B). These results agree well with other studies that have shown decreased Fe-Fe cornersharing linkages when ferrihydrite was co-precipitated with Si, Al, and organic ligands (Cismasu et al., 2012; Cismasu et al., 2014; Mikutta, 2011; ThomasArrigo et al., 2019). A peak at ~1.60 Å present in PDFs for the BIOS samples has been interpreted as mineral surface associated and/or precipitates of tetrahedral silica (Cismasu et al., 2011; Toner et al., 2012), and the broadening and slight shifts in peak position R  $\sim$  1.5 Å for BIOS Fr and FFFD as average distances between bonded (e.g., C-C/N/O) and unbonded atoms in the organic matter (Poulain et al., 2019). These results are consistent with long-range ordering measurements (S-XRD, PDF, and MBS) and suggest BIOS is less ordered than 2LFh, composed of distinct pools of iron (HFO, 2LFh, and organically bound Fe), and that drying treatments cause some ordering and mineralogical changes in BIOS.

We note that the coordination numbers for Fe(III)—O shells from K-edge EXAFS fitting are systematically higher for BIOS (although close to the estimated uncertainty in coordination number or ~20%), which is consistent with L-edge XANES results. These results suggest a more uniform octahedral first shell coordination environment (e.g., no tetrahedral Fe(III)) despite the reduction in structural order seen in other measurements of short- and longrange ordering. It has been shown with synthetic 2LFh that decreasing size may result in a surficial depletion of tetrahedral and corner-sharing sites (Hiemstra, 2013, 2018), a phenomenon that has also been noted with synthetic 2LFhorganic co-precipitates (Mikutta, 2011; ThomasArrigo et al., 2019; Vantelon et al., 2019). Based on both long range (MBS and S-XRD) and short-rage (EXAFS LCFs and structure fitting) evidence, we assert that organic matter is intimately mixed with mineral phases in the BIOS, further contributing to these structural changes. It is thus possible that the decrease in corner sharing and lack of tetrahedral sites in the BIOS may result from extremely small CSD, which may result from rapid formation (Druschel et al., 2008) or poisoning of growth by organic matter (Karlsson and Persson, 2012; ThomasArrigo et al., 2019; Vantelon et al., 2019), or possibly the direct complexation of organic matter, which may cap octahedral edgesharing sites (Karlsson and Persson, 2012; Rose et al., 1998; ThomasArrigo et al., 2019; Vilgé-Ritter et al., 1999). We note that other inorganic impurities (Cismasu et al., 2012; Voegelin et al., 2010), such as silica, phosphate, and aluminum, may also contribute to this effect.

#### 4.3. Structure of BIOS and 2LFh

Overall, a suite of spectroscopic, scattering, and microscopy techniques present cohesive observations that sharply contrast the structure and behaviour of BIOS and 2LFh. For all 2LFh samples, XAS spectra, X-ray diffractograms, PDFs, and MBS spectra showed a consistent trend (Supplementary Table S12) in increased long- and short-range ordering for the 2LFh FrFD and OD sample preparations

when compared to not drying the sample (2LFr Fr). These results are in good agreement with Greffie et al. (Greffié et al., 2001), and Lewis (Lewis, 1992) who showed increases in ferrihydrite ordering after freeze-drying and oven drying, respectively. Fe L-edge XANES spectra showed that the coordination environment of all 2LFh samples were primarily composed of octahedral Fe(III), however, tetrahedral Fe(III) was detected, which agrees well with Fe Ledge XANES (Peak and Regier, 2012), K-edge XANES/ EXAFS (Maillot et al., 2011; Mikutta, 2011), and neutron scattering data (Harrington et al., 2011) that shows tetrahedral Fe(III) values between 13-35% for 2LFh. Sample preparation also impacted the BIOS morphology and structure. When compared to BIOS FrFD, SEM images showed a change in the BIOS OD morphology that is more similar to 2LFh morphology. X-ray diffractograms and EXAFS LCFs suggested an increase in ordering and a decrease in Fe-organic complexes with increasingly aggressive drying (Fr, FFFD, FrFD, OD); MBS spectra also exhibit this trend for all BIOS samples in a decreasing peak hyperfine field strengths (Bhf) from the OD sample (46.5  $\pm$  0.6) and the lowest for the Fr sample (44.7  $\pm$  0.1), with intermediate values obtained for the BIOS FrFD and FFFD samples. The decrease of tetrahedral and corner sharing iron is consistent with the reduced CSD size (from PDF) and the presence of organic matter mixed into phases, as indicated by EXAFS and MBS.

Based on comparisons to 2LFh, we can integrate our mineral structure data with literature observations of morphology and composition to develop a comprehensive model of BIOS deposits in circumneutral freshwater environments (Fig. 8). Our spectroscopic and scattering data collectively illustrates a decrease in both domain size and ordering (both short- and long-range) for all BIOS sample preparations when compared to the 2LFh sample set; the presence of organic matter associated with the mineral structure is also observed by the different structural techniques used here. Substantially lower amounts of tetrahedral Fe(III) and decreased corner sharing sites in BIOS as compared to 2LFh (based on L-edge XANES) also highlights the structural differences between the Fe (oxyhydr) oxides

Although we did not directly probe the cause of these differences, several factors may influence the structure of BIOS. First, to produce BIOS, organisms must outpace inorganic Fe oxidation (even with abiotic contributions) (Druschel et al., 2008), resulting in rapid formation that promotes small domains and disordering. Second, BIOS formation tends to be controlled by its interactions with biopolymers, resulting in distinctive morphologies, and potentially altered structures (Chan et al., 2004; Chan et al., 2009; Sowers et al., 2019); the incorporation of Si, Al, P, and organic C into the structure of the iron (oxyhydr)oxides impedes crystal growth by inhibiting dehydration and atomic rearrangement (Chen et al., 2014; Cismasu et al., 2012; Cismasu et al., 2014; Cismasu et al., 2011; Eusterhues et al., 2008; Mikutta, 2011; Mikutta et al., 2014), contributing to small CSD and poor ordering. The presence of these impurities, especially organic C, and the small crystal size may result in substantial decreases in

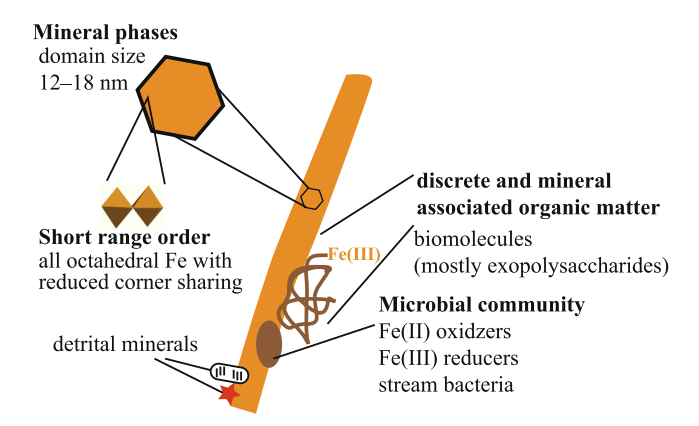


Fig. 8. A model of biogenic iron oxide deposits form in circumneutral aquatic environments. Pair distribution functions (PDF) indicate an exceptionally small coherent scattering domain size. Mössbauer, spectroscopy, Fe K-edge and L-edge X-ray absorption spectroscopy spectra, synchrotron X-ray diffraction (S-XRD) and PDFs indicate a dominant 2LFh-like phase that is predominantly octahedrally coordinated Fe with reduced corner sharing. Additionally, S-XRD suggest the possible presence of Fe-organic complexes, which may be associated with biomolecules (Chan et al., 2004; Chan et al., 2009; Mitsunobu et al., 2012; Sowers et al., 2019; Suga et al., 2017) or detrital carbon (Sowers et al., 2019) associated with these matts. Microbial community structures have been recently reviewed (Emerson et al., 2010; Roden et al., 2012). Although a Fe(III)-(oxyhydr)oxide sheath is depicted, other morphologies (such as balls and stalks) are also commonly observed (Duckworth et al., 2009; Fleming et al., 2013; Spring, 2006).

tetrahedrally coordinated Fe and corner-sharing Fe in the BIOS via surface depletion of higher energy sites or complexation by organics (Hiemstra, 2013, 2018; Mikutta, 2011; ThomasArrigo et al., 2019; Vantelon et al., 2019).

### 5. ENVIRONMENTAL IMPLICATIONS AND CONCLUSION

Results from our diverse set of spectroscopic and scattering techniques collectively show that the structure and coordination geometry of BIOS are substantially different than that of 2LFh in terms of size, ordering, coordination, morphology, and composition. This difference in reactivity is supported by an array of studies that show differences in sorption affinity for Cr(VI) (Whitaker et al., 2018), As(V) (Sowers et al., 2017), Cu (Rentz and Ullman, 2012), Pb (Whitaker and Duckworth, 2018), Zn (Rentz and Ullman, 2012; Whitaker and Duckworth, 2018), I (Kennedy et al., 2011), P (Field et al., 2019), Sr (Langley et al., 2009a), and DOC (Sowers et al., 2019) to BIOS when compared to synthetic 2LFh. Furthermore, possibly due to the presence of organic matter, Si, and P within the BIOS, simulated environmental conditions (e.g., freezing, drying) had little effect on its structure noted by the more aggressive sample preparation, BIOS OD, remaining more poorly ordered with a smaller CSD than the least aggressive synthetic treatment, 2LFh Fr. This suggests that the BIOS are much less likely to transform to more crystalline phases than 2LFh models. This assertion is further supported by Chen et al. (2015), who showed that organic matter could significantly impede the abiotic transformation of ferrihydrite by Fe(II), which may suggest that the structure of BIOS could be highly resilient to phase changes even at redox gradients typical of circumneutral pH environments. However, variations in the EXAFS LCF components and diffraction patterns seen with the more aggressive drying techniques likely indicate a change in BIOS reactivity

(Field et al., 2019) and should be considered when designing future BIOS studies, especially sorption and modelling contaminant fate and transport. Together, these observations suggest that studies of BIOS are a unique component of environmental mineralogy and their structures and reactivities are distinct from 2LFh, with implications for the cycling and mobility of nutrients, metals, organic matter, and other contaminants in similar redox active interfaces.

#### **Declaration of Competing Interest**

The authors declare that they have no known competing financial interests or personal relationships that could have appeared to influence the work reported in this paper.

#### ACKNOWLEDGEMENT

We are grateful for support received from the National Science Foundation Geobiology and Low-Temperature Geochemistry Program (EAR-125515). This research was funded in part by a grant from the National institute of Environmental Health Sciences (P42ES031007). This work was supported by the USDA National Institute of Food and Agriculture, Hatch projects NC02440 and NC02713. This work was supported by the Game-Changing Research Initiative Program (GRIP) through the NC State Office of Research and Innovation (ORI), RTI International, and the Kenan Institute for Engineering, Science and Technology. We thank Tyler Sowers, Joshua Henson, Ryan Davis, Dean Hesterberg, Kim Hutchison, and Lisa Lentz for their assistance on this project. This work was performed in part at the Environmental and Agricultural Testing Service laboratory (EATS), Department of Crop and Soil Sciences, at North Carolina State University and the Analytical Instrumentation Facility (AIF) at North Carolina State University, which is supported by the State of North Carolina and the National Science Foundation (award number ECCS-1542015). The AIF is a member of the North Carolina Research Triangle Nanotechnology Network (RTNN), a site in the National Nanotechnology Coordinated Infrastructure (NNCI). Use of the Stanford Synchrotron Radiation Lightsource, SLAC National Accelerator Laboratory, is supported by the U.S. Department of Energy, Office of Science, and Office of Basic Energy Sciences under Contract No. DE-AC02-76SF00515. Part of the research described in this paper was performed at the Canadian Light Source, a national research facility of the University of Saskatchewan, which is supported by the Canada Foundation for Innovation (CFI), the Natural Sciences and Engineering Research Council (NSERC), the National Research Council (NRC), the Canadian Institutes of Health Research (CIHR), the Government of Saskatchewan, and the University of Saskatchewan. This research used resources of the Advanced Photon Source, a U.S. Department of Energy (DOE) Office of Science User Facility operated for the DOE Office of Science by Argonne National Laboratory under Contract No. DE-AC02-06CH11357.

#### APPENDIX A. SUPPLEMENTARY MATERIAL

Supplementary data to this article can be found online at https://doi.org/10.1016/j.gca.2021.05.059.

#### REFERENCES

- Achkar A., Regier T., Wadati H., Kim Y.-J., Zhang H. and Hawthorn D. (2011) Bulk sensitive x-ray absorption spectroscopy free of self-absorption effects. *Phys. Rev. B Condens. Matter* 83, 081106.
- Almaraz N., Whitaker A. H., Andrews M. Y. and Duckworth O. W. (2017) Assessing biomineral formation by iron-oxidizing bacteria in a circumneutral creek. J. Contemp. Water Res. Educ. 160, 60–71.
- Benjamin M. M. and Leckie J. O. (1981) Multiple-site adsorption of Cd, Cu, Zn, and Pb on amorphous iron oxyhydroxide. *J. Colloid Interface Sci.* **79**, 209–221.
- Chadwick J., Jones D., Thomas M., Tatlock G. and Devenish R. (1986) A Mössbauer study of ferrihydrite and aluminium substituted ferrihydrites. *J. Magn. Magn. Mater.* **61**, 88–100.
- Chan C. S., De Stasio G., Welch S. A., Girasole M., Frazer B. H., Nesterova M. V., Fakra S. and Banfield J. F. (2004) Microbial polysaccharides template assembly of nanocrystal fibers. *Science* **303**, 1656–1658.
- Chan C. S., Fakra S. C., Edwards D. C., Emerson D. and Banfield J. F. (2009) Iron oxyhydroxide mineralization on microbial extracellular polysaccharides. *Geochim. Cosmochim. Acta* 73, 3807–3818.
- Chen C., Dynes J. J., Wang J. and Sparks D. L. (2014) Properties of Fe-organic matter associations via coprecipitation versus adsorption. *Environ. Sci. Technol.* 48, 13751–13759.
- Chen C., Kukkadapu R. and Sparks D. L. (2015) Influence of coprecipitated organic matter on Fe2+ (aq)-catalyzed transformation of ferrihydrite: implications for carbon dynamics. *Environ. Sci. Technol.* 49, 10927–10936.
- Chen C., Meile C., Wilmoth J., Barcellos D. and Thompson A. (2018) Influence of pO<sub>2</sub> on iron redox cycling and anaerobic organic carbon mineralization in a humid tropical forest soil. *Environ. Sci. Technol.* **52**, 7709–7719.
- Chen C. and Thompson A. (2018) Ferrous iron oxidation under varying pO<sub>2</sub> levels: The effect of Fe(III)/Al(III) oxide minerals and organic matter. *Environ. Sci. Technol.* **52**, 597–606.
- Cismasu A. C., Levard C., Michel F. M. and Brown G. E. (2013) Properties of impurity-bearing ferrihydrite II: Insights into the surface structure and composition of pure, Al- and Si-bearing ferrihydrite from Zn(II) sorption experiments and Zn K-edge X-ray absorption spectroscopy. *Geochim. Cosmochim. Acta* 119, 46–60.

- Cismasu A. C., Michel F. M., Stebbins J. F., Levard C. and Brown G. E. (2012) Properties of impurity-bearing ferrihydrite I. Effects of Al content and precipitation rate on the structure of 2-line ferrihydrite. *Geochim. Cosmochim. Acta* 92, 275–291.
- Cismasu A. C., Michel F. M., Tcaciuc A. P. and Brown G. E. (2014) Properties of impurity-bearing ferrihydrite III. Effects of Si on the structure of 2-line ferrihydrite. *Geochim. Cosmochim. Acta* 133, 168–185.
- Cismasu A. C., Michel F. M., Tcaciuc A. P., Tyliszczak T. and Brown, Jr, G. E. (2011) Composition and structural aspects of naturally occurring ferrihydrite. *C. R. Geosci.* **343**, 210–218.
- Combes J., Manceau A. and Calas G. (1990) Formation of ferric oxides from aqueous solutions: A polyhedral approach by Xray absorption spectroscopy: II. Hematite formation from ferric gels. *Geochim. Cosmochim. Acta* 54, 1083–1091.
- Combes J., Manceau A., Calas G. and Bottero J. (1989) Formation of ferric oxides from aqueous solutions: A polyhedral approach by X-ray absorption spectroscdpy: I. Hydrolysis and formation of ferric gels. *Geochim. Cosmochim. Acta* 53, 583–594.
- Cornell R. M. and Schwertmann U. (2003) *The Iron Oxides:* Structure, Properties, Reactions, Occurrences and Uses. John Wiley & Sons.
- Coward E. K., Thompson A. and Plante A. F. (2018) Contrasting Fe speciation in two humid forest soils: Insight into organomineral associations in redox-active environments. *Geochim. Cosmochim. Acta* 238, 68–84.
- Crocombette J., Pollak M., Jollet F., Thromat N. and Gautier-Soyer M. (1995) X-ray-absorption spectroscopy at the Fe L 2, 3 threshold in iron oxides. *Phys. Rev. B Condens. Matter* **52**, 3143.
- Downward L., Booth C. H., Lukens W. W. and Bridges F. (2007) A variation of the F-test for determining statistical relevance of particular parameters in EXAFS fits. AIP Conf. Proc. 882, 129– 131.
- Drits V., Sakharov B., Salyn A. and Manceau A. (1993) Structural model for ferrihydrite. Clay Miner. 28, 185–185.
- Druschel G. K., Emerson D., Sutka R., Suchecki P. and Luther, G. W. (2008) Low-oxygen and chemical kinetic constraints on the geochemical niche of neutrophilic iron (II) oxidizing microorganisms. *Geochim. Cosmochim. Acta* 72, 3358–3370.
- Duckworth O. W., Holmstrom S. J. M., Pena J. and Sposito G. (2009) Biogeochemistry of iron oxidation in a circumneutral freshwater habitat. *Chem. Geol.* 260, 149–158.
- Emerson D., Fleming E. and McBeth J. (2010) Iron-Oxidizing Bacteria: An environmental and genomic perspective. *Ann. Rev. Microbiol.* **64**, 561–583.
- Emerson D. and Moyer C. (1997) Isolation and characterization of novel iron-oxidizing bacteria that grow at circumneutral pH. *Appl. Environ. Microbiol.* **63**, 4784–4792.
- Emerson D. and Moyer C. L. (2002) Neutrophilic Fe-oxidizing bacteria are abundant at the Loihi Seamount hydrothermal vents and play a major role in Fe oxide deposition. *Appl. Environ. Microbiol.* **68**, 3085–3093.
- Emerson D. and Revsbech N. P. (1994a) Investigation of an ironoxidizing microbial mat community located near Aarhus, Denmark: field studies. *Appl. Environ. Microbiol.* 60, 4022– 4031.
- Emerson D. and Revsbech N. P. (1994b) Investigation of an iron-oxidizing microbial mat community located near Aarhus, Denmark: laboratory studies. Appl. Environ. Microbiol. 60, 4032–4038
- Emerson D. and Weiss J. V. (2004) Bacterial iron oxidation in circumneutral freshwater habitats: findings from the field and the laboratory. *Geomicrobiol. J.* **21**, 405–414.
- Eusterhues K., Wagner F. E., Häusler W., Hanzlik M., Knicker H., Totsche K. U., Kögel-Knabner I. and Schwertmann U. (2008)

- Characterization of ferrihydrite-soil organic matter coprecipitates by X-ray diffraction and Mossbauer spectroscopy. *Environ. Sci. Technol.* **42**, 7891–7897.
- Ferris F. (2005) Biogeochemical properties of bacteriogenic iron oxides. *Geomicrobiol. J.* **22**, 79–85.
- Ferris F., Hallberg R., Lyven B. and Pedersen K. (2000) Retention of strontium, cesium, lead and uranium by bacterial iron oxides from a subterranean environment. *Appl. Geochem.* **15**, 1035–1042.
- Field H. R., Whitaker A. H., Henson J. A. and Duckworth O. W. (2019) Sorption of copper and phosphate to diverse biogenic iron (oxyhydr)oxide deposits. Sci. Total Environ. 697, 134111.
- Fleming E. J., Cetinić I., Chan C. S., Whitney King D. and Emerson D. (2013) Ecological succession among iron-oxidizing bacteria. *Isme J.* 8, 804.
- Fleming E. J., Langdon A. E., Martinez-Garcia M., Stepanauskas R., Poulton N. J., Masland E. D. P. and Emerson D. (2011) What's new is old: Resolving the identity of *Leptothrix ochracea* using single cell genomics, pyrosequencing and FISH. *PLOS ONE* **6**, e17769.
- Gilbert B., Huang F., Zhang H., Waychunas G. A. and Banfield J. F. (2004) Nanoparticles: strained and stiff. *Science* 305, 651–654.
- Ginn B., Meile C., Wilmoth J., Tang Y. and Thompson A. (2017) Rapid iron reduction rates are stimulated by high-amplitude redox fluctuations in a tropical forest soil. *Environ. Sci. Technol.* 51, 3250–3259.
- Greffié C., Amouric M. and Parron C. (2001) HRTEM study of freeze-dried and untreated synthetic ferrihydrites: consequences of sample processing. *Clay Miner.* **36**, 381–387.
- Guénet H., Davranche M., Vantelon D., Gigault J., Prévost S., Taché O., Jaksch S., Pédrot M., Dorcet V., Boutier A. and Jestin J. (2017) Characterization of iron-organic matter nanoaggregate networks through a combination of SAXS/SANS and XAS analyses: impact on As binding. *Environ. Sci. Nano* 4, 938–954.
- Hall B., Zanchet D. and Ugarte D. (2000) Estimating nanoparticle size from diffraction measurements. J. Appl. Crystallogr. 33, 1335–1341.
- Hamilton W. C. (1965) Significance tests on the crystallographic R factor. *Acta. Crystallogr.* **18**, 502–510.
- Hammersley, A., 1997. FIT2D: an introduction and overview. European Synchrotron Radiation Facility Internal Report ESRF97HA02T, p. 58.
- Harrington J. M., Bargar J. M., Jarzecki A. A., Sombers L. A., Roberts J. G. and Duckworth O. W. (2012a) Trace metal complexation by the triscatecholate siderophore protochelin: structure and stability. *BioMetals* 25, 393–412.
- Harrington J. M., Parker D. L., Bargar J. R., Jarzecki A. A., Tebo B. M., Sposito G. and Duckworth O. W. (2012b) Structural dependence of Mn complexation by siderophores: donor group dependence on complex stability and reactivity. *Geochim. Cosmochim. Acta* 88, 106–119.
- Harrington R., Hausner D. B., Xu W., Bhandari N., Michel F. M., Brown G. E., Strongin D. R. and Parise J. B. (2011) Neutron pair distribution function study of two-line ferrihydrite. *Envi*ron. Sci. Technol. 45, 9883–9890.
- Herndon E. M., Kinsman-Costello L., Duroe K. A., Mills J., Kane E. S., Sebestyen S. D., Thompson A. A. and Wullschleger S. D. (2019) Iron (oxyhydr)oxides serve as phosphate traps in tundra and boreal peat soils. J. Geophys. Res. Biogeosci. 124, 227–246.
- Hiemstra T. (2013) Surface and mineral structure of ferrihydrite. *Geochim. Cosmochim. Acta* **105**, 316–325.
- Hiemstra T. (2018) Surface structure controlling nanoparticle behavior: magnetism of ferrihydrite, magnetite, and maghemite. *Environ. Sci. Nano* 5, 752–764.

- Houot S. and Berthelin J. (1992) Submicroscopic studies of iron deposits occurring in field drains: formation and evolution. *Geoderma* **52**, 209–222.
- Jambor J. L. and Dutrizac J. E. (1998) Occurrence and constitution of natural and synthetic ferrihydrite, a widespread iron oxyhydroxide. *Chem. Rev.* 98, 2549–2586.
- Jensen C. M. and Lee D. W. (2000) Dry-ice bath based on ethylene glycol mixtures. J. Chem. Educ. 77, 629.
- Jones J. (1975) Some observations on the occurrence of the iron bacterium Leptothrix ochracea in fresh water, including reference to large experimental enclosures. J. Appl. Bact. 39, 63–72.
- Juhás P., Davis T., Farrow C. L. and Billinge S. J. (2013) PDFgetX3: a rapid and highly automatable program for processing powder diffraction data into total scattering pair distribution functions. J. Appl. Crystallogr. 46, 560–566.
- Kahle M., Kleber M. and Jahn R. (2002) Carbon storage in loess derived surface soils from Central Germany: Influence of mineral phase variables. J. Plant. Nutr. Soil Sci. 165, 141–149.
- Karlsson T. and Persson P. (2012) Complexes with aquatic organic matter suppress hydrolysis and precipitation of Fe(III). *Chem. Geol.* 322–323, 19–27.
- Kelly S., Hesterberg D. and Ravel B. (2008) Analysis of soils and minerals using X-ray absorption spectroscopy. *Methods Soil Anal. Part.* 387–463.
- Kennedy C., Gault A., Fortin D., Clark I. and Ferris F. (2011) Retention of iodide by bacteriogenic iron oxides. *Geomicrobiol.* J. 28, 387–395.
- Kennedy C., Martinez R., Scott S. D. and Ferris F. (2003) Surface chemistry and reactivity of bacteriogenic iron oxides from Axial Volcano, Juan de Fuca Ridge, north-east Pacific Ocean. *Geobiology* 1, 59–69.
- Kiem R. and Kögel-Knabner I. (2002) Refractory organic carbon in particle-size fractions of arable soils II: organic carbon in relation to mineral surface area and iron oxides in fractions <6 μm. *Org. Geochem.* **33**, 1699–1713.
- Kikuchi S., Kashiwabara T., Shibuya T. and Takahashi Y. (2019) Molecular-scale insights into differences in the adsorption of cesium and selenium on biogenic and abiogenic ferrihydrite. *Geochim. Cosmochim. Acta* **251**, 1–14.
- Langley S., Gault A. G., Ibrahim A., Takahashi Y., Renaud R., Fortin D., Clark I. D. and Ferris F. G. (2009a) Sorption of strontium onto bacteriogenic iron oxides. *Environ. Sci. Technol.* 43, 1008–1014.
- Langley S., Igric P., Takahashi Y., Sakai Y., Fortin D., Hannington M. and Schwarz-Schampera U. (2009b) Preliminary characterization and biological reduction of putative biogenic iron oxides (BIOS) from the Tonga-Kermadec Arc, southwest Pacific Ocean. *Geobiology* 7, 35–49.
- Larese-Casanova P., Cwiertny D. M. and Scherer M. M. (2010) Nanogoethite formation from oxidation of Fe(II) sorbed on aluminum oxide: implications for contaminant reduction. *Environ. Sci. Technol.* 44, 3765–3771.
- Lewis D. G. (1992) Transformations induced in ferrihydrite by oven-drying. *J. Plant. Nutr. Soil Sci.* **155**, 461–466.
- Liu Y.-T. and Hesterberg D. (2011) Phosphate bonding on noncrystalline Al/Fe-hydroxide coprecipitates. *Environ. Sci. Technol.* 45, 6283–6289.
- Lünsdorf H., Brümmer I., Timmis K. and Wagner-Döbler I. (1997) Metal selectivity of in situ microcolonies in biofilms of the Elbe river. J. Bacteriol. 179, 31–40.
- Maillot F., Morin G., Wang Y., Bonnin D., Ildefonse P., Chaneac C. and Calas G. (2011) New insight into the structure of nanocrystalline ferrihydrite: EXAFS evidence for tetrahedrally coordinated iron (III). *Geochim. Cosmochim. Acta* 75, 2708–2720.

- Manceau A. (2009) Evaluation of the structural model for ferrihydrite derived from real-space modelling of high-energy X-ray diffraction data. Clay Miner. 44, 19–34.
- Manceau A. (2010) PDF analysis of ferrihydrite and the violation of Pauling's Principia. *Clay Miner.* **45**, 225–228.
- Manceau A. and Drits V. (1993) Local structure of ferrihydrite and feroxyhite by EXAFS spectroscopy. *Clay Miner.* **28**, 165–165.
- Manceau A. and Gates W. (1997) Surface structural model for ferrihydrite. Clays Clay Miner. 45, 448–460.
- Michel F. M. (2014) Total scattering studies of natural and synthetic ferrihydrite. In *Advanced Applications of Synchrotron Radiation in Clay Science*. Clay Minerals Society, pp. 89–135.
- Michel F. M., Barrón V., Torrent J., Morales M. P., Serna C. J.,
  Boily J.-F., Liu Q., Ambrosini A., Cismasu A. C. and Brown G.
  E. (2010a) Ordered ferrimagnetic form of ferrihydrite reveals links among structure, composition, and magnetism. *Proc. Natl. Acad. Sci. U.S.A.* 107, 2787–2792.
- Michel F. M., Ehm L., Antao S. M., Lee P. L., Chupas P. J., Liu G., Strongin D. R., Schoonen M. A., Phillips B. L. and Parise J. B. (2007a) The structure of ferrihydrite, a nanocrystalline material. *Science* 316, 1726–1729.
- Michel F. M., Ehm L., Liu G., Han W., Antao S., Chupas P., Lee P., Knorr K., Eulert H. and Kim J. (2007b) Similarities in 2-and 6-line ferrihydrite based on pair distribution function analysis of X-ray total scattering. *Chem. Mater.* **19**, 1489–1496.
- Michel F. M., Hosein H.-A., Hausner D. B., Debnath S., Parise J. B. and Strongin D. R. (2010b) Reactivity of ferritin and the structure of ferritin-derived ferrihydrite. *Biochim. Biophys. Acta Gen. Subj.* 1800, 871–885.
- Mikutta C. (2011) X-ray absorption spectroscopy study on the effect of hydroxybenzoic acids on the formation and structure of ferrihydrite. *Geochim. Cosmochim. Acta* 75, 5122–5139.
- Mikutta R., Lorenz D., Guggenberger G., Haumaier L. and Freund A. (2014) Properties and reactivity of Fe-organic matter associations formed by coprecipitation versus adsorption: Clues from arsenate batch adsorption. *Geochim. Cosmochim. Acta* 144, 258–276.
- Mitsunobu S., Shiraishi F., Makita H., Orcutt B. N., Kikuchi S., Jorgensen B. B. and Takahashi Y. (2012) Bacteriogenic Fe (III) (oxyhydr) oxides characterized by synchrotron microprobe coupled with spatially resolved phylogenetic analysis. *Environ.* Sci. Technol. 46, 3304–3311.
- Morris A. J. and Hesterberg D. L. (2012) Iron(III) coordination and phosphate sorption in peat reacted with ferric or ferrous iron. Soil Sci. Soc. Am. J. 76, 101–109.
- Neubauer S. C., Emerson D. and Megonigal J. P. (2002) Life at the energetic edge: kinetics of circumneutral iron oxidation by lithotrophic iron-oxidizing bacteria isolated from the wetlandplant rhizosphere. *Appl. Environ. Microbiol.* 68, 3988–3995.
- Newville M. (2001) IFEFFIT: interactive XAFS analysis and FEFF fitting. *J. Synchrotron Radiat.* **8**, 322–324.
- Norrman B. (1993) Filtration of water samples for DOC studies. Mar. Chem. 41, 239–242.
- O'Day P. A., Rivera, Jr, N., Root R. and Carroll S. A. (2004) X-ray absorption spectroscopic study of Fe reference compounds for the analysis of natural sediments. *Am. Mineral.* **89**, 572–585.
- Peak D. and Regier T. (2012) Direct observation of tetrahedrally coordinated Fe (III) in ferrihydrite. *Environ. Sci. Technol.* 46, 3163–3168.
- Poggenburg C., Mikutta R., Sander M., Schippers A., Marchanka A., Dohrmann R. and Guggenberger G. (2016) Microbial reduction of ferrihydrite-organic matter coprecipitates by Shewanella putrefaciens and Geobacter metallireducens in comparison to mediated electrochemical reduction. *Chem. Geol.* 447, 133–147.

- Poulain A., Dupont C., Martinez P., Guizani C. and Drnec J. (2019) Wide-angle X-ray scattering combined with pair distribution function analysis of pyrolyzed wood. J. Appl. Crystallogr. 52, 60-71.
- Prigsheim E. G. (1949) The filamentous bacteria Spaerotilus, Leptothrix, Cladothrix, and their relation to iron and manganese. Phlos. T. Rov. Soc. B. 233, 453–482.
- Rancourt D. and Meunier J.-F. (2008) Constraints on structural models of ferrihydrite as a nanocrystalline material. Am. Mineral. 93, 1412–1417.
- Rancourt D. and Ping J. (1991) Voigt-based methods for arbitraryshape static hyperfine parameter distributions in Mössbauer spectroscopy. Nucl. Instrum. Methods Phys. Res B 58, 85–97.
- Rancourt D. G., Thibault P.-J., Mavrocordatos D. and Lamarche G. (2005) Hydrous ferric oxide precipitation in the presence of nonmetabolizing bacteria: Constraints on the mechanism of a biotic effect. *Geochim. Cosmochim. Acta* 69, 553–577.
- Rasmussen C., Heckman K., Wieder W. R., Keiluweit M., Lawrence C. R., Berhe A. A., Blankinship J. C., Crow S. E., Druhan J. L., Hicks Pries C. E., Marin-Spiotta E., Plante A. F., Schädel C., Schimel J. P., Sierra C. A., Thompson A. and Wagai R. (2018) Beyond clay: towards an improved set of variables for predicting soil organic matter content. *Biogeo-chemistry* 137, 297–306.
- Rehr J. J., Kas J. J., Vila F. D., Prange M. P. and Jorissen K. (2010) Parameter-free calculations of X-ray spectra with FEFF9. *Phys. Chem. Chem. Phys.* **12**, 5503–5513.
- Rentz J. A., Turner I. P. and Ullman J. L. (2009) Removal of phosphorus from solution using biogenic iron oxides. Water Res. 43, 2029–2035.
- Rentz J. A. and Ullman U. (2012) Copper and zinc removal using biogenic iron oxides. In World Environmental and Water Resources Congress 2012 (ed. E. D. Loucks), pp. 687–698.
- Roden E., McBeth J. M., Blothe M., Percak-Dennett E. M., Fleming E. J., Holyoke R. R., Luther G. W. and Emerson D. (2012) The microbial ferrous wheel in a neutral pH groundwater seep. Front. Microbiol. 3.
- Roden E. E. (2012) Microbial iron-redox cycling in subsurface environments. *Biochem. Soc. Trans.* 40, 1249–1256.
- Rose J., Vilge A., Olivie-Lauquet G., Masion A., Frechou C. and Bottero J. Y. (1998) Iron speciation in natural organic matter colloids. *Colloids Surf A Physicochem. Eng. Asp.* 136, 11–19.
- Schaefer M. V., Gorski C. A. and Scherer M. M. (2011) Spectroscopic evidence for interfacial Fe (II) – Fe (III) electron transfer in a clay mineral. *Environ. Sci. Technol.* 45, 540–545.
- Schwertmann U. and Cornell R. M. (2008) Iron Oxides in the Laboratory: Preparation and Characterization. John Wiley & Sons.
- Shannon R. D. (1976) Revised effective ionic radii and systematic studies of interatomic distances in halides and chalcogenides. *Acta. Crystall. A-Crys.* **32**, 751–767.
- Sheldon S. P. and Skelly D. K. (1990) Differential colonization and growth of algae and ferromanganese-depositing bacteria in a mountain stream. J. Freshw. Ecol. 5, 475–485.
- Sowers T. D., Harrington J. M., Polizzotto M. L. and Duckworth O. W. (2017) Sorption of arsenic to biogenic iron (oxyhydr) oxides produced in circumneutral environments. *Geochim. Cosmochim. Acta* 198, 194–207.
- Sowers T. D., Holden K. L., Coward E. K. and Sparks D. L. (2019) Dissolved organic matter sorption and molecular fractionation by naturally occurring bacteriogenic iron (oxyhydr)oxides. *Environ. Sci. Technol.* 53, 4295–4304.
- Spring S. (2006) The genera Lepthothrix and Sphaerotilus. Prokarvotes 5, 758–777.
- Stookey L. L. (1970) Ferrozine a new spectrophotometric reagent for iron. Anal. Chem. 42, 779–781.

- Suga H., Kikuchi S., Takeichi Y., Miyamoto C., Miyahara M., Mitsunobu S., Ohigashi T., Mase K., Ono K. and Takahashi Y. (2017) Spatially resolved distribution of Fe species around microbes at the submicron scale in natural bacteriogenic iron oxides. *Microbes Environ.* 32, 283–287.
- Swanner E. D., Nell R. M. and Templeton A. S. (2011) Ralstonia species mediate Fe-oxidation in circumneutral, metal-rich subsurface fluids of Henderson mine, CO. *Chem. Geol.* 284, 339–350.
- ThomasArrigo L. K., Kaegi R. and Kretzschmar R. (2019) Ferrihydrite growth and transformation in the presence of ferrous iron and model organic ligands. *Environ. Sci. Technol.* 53, 13636–13647.
- ThomasArrigo L. K., Mikutta C., Byrne J., Barmettler K., Kappler A. and Kretzschmar R. (2014) Iron and arsenic speciation and distribution in organic flocs from streambeds of an arsenic-enriched peatland. *Environ. Sci. Technol.* 48, 13218–13228.
- Thompson A., Rancourt D. G., Chadwick O. A. and Chorover J. (2011) Iron solid-phase differentiation along a redox gradient in basaltic soils. *Geochim. Cosmochim. Acta* **75**, 119–133.
- Toner B. M., Berquó T. S., Michel F. M., Sorensen J. V., Templeton A. S. and Edwards K. J. (2012) Mineralogy of iron microbial mats from Loihi Seamount. Front. Microbiol. 3.
- Toner B. M., Santelli C. M., Marcus M. A., Wirth R., Chan C. S., McCollom T., Bach W. and Edwards K. J. (2009) Biogenic iron oxyhydroxide formation at mid-ocean ridge hydrothermal vents: Juan de Fuca Ridge. *Geochim. Cosmochim. Acta* 73, 388–403.
- Torn M. S., Trumbore S. E., Chadwick O. A., Vitousek P. M. and Hendricks D. M. (1997) Mineral control of soil organic carbon storage and turnover. *Nature* **389**, 170.
- Tuhela L., Carlson L. and Tuovinen O. H. (1997) Biogeochemical transformations of Fe and Mn in oxic groundwater and well water environments. *J. Environ. Sci. Health A Tox. Hazard. Subst. Environ. Eng.* **32**, 407–426.
- Vantelon D., Davranche M., Marsac R., La Fontaine C., Guénet H., Jestin J., Campaore G., Beauvois A. and Briois V. (2019) Iron speciation in iron-organic matter nanoaggregates: a kinetic approach coupling Quick-EXAFS and MCR-ALS chemometrics. *Environ. Sci. Nano* 6, 2641–2651.
- Vilgé-Ritter A., Rose J., Masion A., Bottero J. Y. and Lainé J. M. (1999) Chemistry and structure of aggregates formed with Fesalts and natural organic matter. *Colloids Surf. A Physicochem. Eng. Asp.* 147, 297–308.

- Voegelin A., Kaegi R., Frommer J., Vantelon D. and Hug S. J. (2010) Effect of phosphate, silicate, and Ca on Fe(III)-precipitates formed in aerated Fe(II)- and As(III)-containing water studied by X-ray absorption spectroscopy. Geochim. Cosmochim. Acta 74, 164–186.
- Wagai R. and Mayer L. M. (2007) Sorptive stabilization of organic matter in soils by hydrous iron oxides. *Geochim. Cosmochim.* Acta 71, 25–35.
- Wang X., Zhu M., Koopal L. K., Li W., Xu W., Liu F., Zhang J., Liu Q., Feng X. and Sparks D. L. (2016) Effects of crystallite size on the structure and magnetism of ferrihydrite. *Environ.* Sci. Nano 3, 190–202.
- Waychunas G. A., Kim C. S. and Banfield J. F. (2005) Nanoparticulate iron oxide minerals in soils and sediments: unique properties and contaminant scavenging mechanisms. *J. Nanopart. Res.* 7, 409–433.
- Webb S. (2005) SIXpack: a graphical user interface for XAS analysis using IFEFFIT. Phys. Scr. 2005, 1011.
- Weiss J. V., Emerson D. and Megonigal J. P. (2005) Rhizosphere iron (III) deposition and reduction in a Juncus effusus L.dominated wetland. Soil Sci. Soc. Am. J. 69, 1861–1870.
- Whitaker A. H. and Duckworth O. W. (2018) Cu, Pb, and Zn sorption to biogenic iron (oxyhydr) oxides formed in circumneutral environments. *Soil Syst.* 2, 18.
- Whitaker A. H., Peña J., Amor M. and Duckworth O. W. (2018) Cr(VI) uptake and reduction by biogenic iron (oxyhydr) oxides. *Environ. Sci. Process. Impacts* **20**, 1056–1068.
- Williams A. G. B. and Scherer M. M. (2004) Spectroscopic evidence for Fe(II)–Fe(III) electron transfer at the iron oxide–water interface. *Environ. Sci. Technol.* **38**, 4782–4790.
- Winkler P., Kaiser K., Thompson A., Kalbitz K., Fiedler S. and Jahn R. (2018) Contrasting evolution of iron phase composition in soils exposed to redox fluctuations. *Geochim. Cos*mochim. Acta 235, 89–102.
- Xu P., Zeng G. M., Huang D. L., Feng C. L., Hu S., Zhao M. H., Lai C., Wei Z., Huang C. and Xie G. X. (2012) Use of iron oxide nanomaterials in wastewater treatment: a review. Sci. Total Environ. 424, 1–10.
- Zhao J., Huggins F. E., Feng Z. and Huffman G. P. (1994) Ferrihydrite: surface structure and its effects on phase transformation. *Clays Clay Miner.* **42**, 737–746.

Associate editor: Juan Liu